Parvovirus infection affects host cell nucleolar organization and ribosome biogenesis

Moona Huttunen[1*], Satu Hakanen[1*], Vesa Aho[1], Simon Leclerc[1], Aynur Soenmez[2], Sergey Kapishnikov[3], Alessandro Zannotti[3], Visa Ruokolainen[1], Kari Salokas[4], Markku Varjosalo[4], Leena Latonen[5], Colin R Parrish[6], Kenneth Fahy[3], Salla Mattola[1], Denis L.J. Lafontaine[2*#], and Maija Vihinen-Ranta[1*#].

[1] Department of Biological and Environmental Science and Nanoscience Center, University of Jyvaskyla, Jyvaskyla, Finland
[2] RNA Molecular Biology, Fonds de la Recherche Scientifique (F.R.S./FNRS), Université libre de Bruxelles (ULB), Biopark campus, B-6041, Gosselies, Belgium
[3]SiriusXT Limited, Dublin, Ireland
[4]Institute of Biotechnology and Helsinki Institute of Life Science (HiLIFE), University of Helsinki, Helsinki, Finland
[5]Institute of Biomedicine, University of Eastern Finland, 70211 Kuopio, Finland
[6]Baker Institute for Animal Health, Department of Microbiology and Immunology, College of Veterinary Medicine, Cornell University, Ithaca, USA

[*]These authors contributed equally to this work.

#Address correspondence to

Denis L.J. Lafontaine, denis.lafontaine@ulb.be
Université libre de Bruxelles (ULB), Fonds de la Recherche Scientifique (F.R.S./FNRS)
Biopark campus, Rue Profs Jeener & Brachet, 12 B-6041 Gosselies, Belgium
Phone: +32 473 973 962

Maija Vihinen-Ranta, maija.vihinen-ranta@jyu.fi
University of Jyvaskyla, Department of Biological and Environmental Science and Nanoscience Center, P.O. Box 35, FI-40014 University of Jyvaskyla, Finland. Phone: +358 400 248 118

Subjects: Nucleolus, ribosome biogenesis, viruses

Running Title: Nucleolar changes in parvoviral infection

Keywords: Nucleolus, ribosome biogenesis, rRNA processing, nucleolar proteins, parvovirus, viral nonstructural NS2 protein

Abstract

The nucleolus is a biomolecular condensate essential for ribosome biogenesis and cellular stress response, and it is a key target for many DNA viruses. However, little is known about how autonomous parvovirus infection impacts nucleolar structure and function. Here, we used advanced imaging techniques, including ten-fold robust expansion microscopy (TREx), cryo soft X-ray tomography (Cryo-SXT), and interactomics and biochemical approaches, to study nucleolar remodeling during canine parvovirus infection. Infection led to redistribution of nucleolar upstream binding transcription factor 1 (inner core), fibrillarin (middle layer), and Ki-67 (outer rim). In contrast, peripheral nucleolar proteins (nucleolin and nucleophosmin) and precursor ribosomal RNAs (pre-rRNAs) remain in circularized structures. TREx and Cryo-SXT microscopy revealed profound nucleolar structural changes, including thickened perinucleolar chromatin and enlarged nucleolar low-protein density channels. BioID identified interactions between viral NS2 and nucleolar proteins in ribosome biogenesis. Northern blotting demonstrated a slowdown in ribosome biogenesis during infection. Collectively, these findings provide novel insights into how parvoviruses remodel nucleolar structure and function.

Introduction

Interaction with a multifunctional subnuclear compartment, the nucleolus, is crucial for the replication and pathogenesis of several DNA viruses, including herpesviruses (Boyne and Whitehouse, 2009; Pearson et al., 2011) and adenoviruses (Lee et al., 2003; Hindley et al., 2007; Lawrence et al., 2006). Moreover, the capsids of adeno-associated virus (AAV), a helper-dependent parvovirus, are assembled in the nucleolus (Wistuba et al., 1997; Johnson and Samulski, 2009). The role of nucleoli in the autonomous parvovirus life cycle has remained unexplored.

The nucleolus is the largest nuclear subcompartment, and it is involved in the initial steps of ribosome biogenesis, such as transcription of ribosomal RNA genes (rRNA), processing and modification of precursor rRNAs (pre-rRNAs), and ribosome subunit assembly (Dubois and Boisvert, 2016; Raska et al., 2006). The events of ribosome production are most likely coordinated, at least in part, by liquid-liquid phase separation (Lafontaine, 2019; Yao et al., 2019). The nucleolus is surrounded by heterochromatin and euchromatin, forming a stable nucleolus-nucleoplasm interface around the nucleoli (Qi and Zhang, 2021; Padeken and Heun, 2014; Caragine et al., 2019; Peng et al., 2023). The mammalian nucleolus comprises three main morphological components: the fibrillar center (FC), the dense fibrillar component (DFC), and the granular component (GC) (Pederson, 2011; Hernandez-Verdun, 2011; Raska et al., 2006; Shan et al., 2023; Lafontaine, 2023a; b). Additional subphases have recently been identified by high-resolution fluorescence microscopy, including the periphery of the dense fibrillar center (PDFC) and the nucleolar rim (NR) (Shan et al., 2023; Stenström et al., 2020). FCs and DFCs are involved in rDNA transcription and initial maturation of pre-rRNAs, whereas further processing of pre-rRNAs and assembly of ribosome subunits occur in GC (Pederson, 2011; Hernandez-Verdun, 2011; Raska et al., 2006). The nucleolus is a dynamic structure (Feric et

al., 2016; Falahati and Wieschaus, 2017; Lafontaine et al., 2021; Strom and Brangwynne, 2019) with highly mobile proteins constantly shuttling between the nucleolus and the nucleoplasm (Phair and Misteli, 2000; Andersen et al., 2005). The nucleolus has many additional functions besides ribosomal biogenesis, including the regulation of mitosis and the cell cycle and acting as a biosensor of stresses of different origins, such as oxidative stress, heat shock, nutrient deprivation, and viral infection (Boisvert et al., 2007; Iarovaia et al., 2019; Boulon et al., 2010; Scherl et al., 2002; Salvetti and Greco, 2014).

The proper localization of several nucleolar proteins is profoundly affected by viral infection. In healthy cells, upstream-binding factor 1 (UBF1), fibrillarin (FBL), nucleolin (NCL), nucleophosmin 1 (NPM1), and proliferation marker protein Ki-67 are enriched in the nucleolar compartments FC, DFC, PDFC, GC, and NR, respectively (Lafontaine et al., 2021; Stenström et al., 2020). In infected cells, some of these proteins are displaced and even relocated outside of the organelle (Callé et al., 2008; Lymberopoulos and Pearson, 2007; Greco et al., 2012). One remarkable example is the abundant multifunctional phosphoprotein NCL (Biggiogera et al., 1990; Ginisty et al., 1999; Srivastava and Pollard, 1999), which relocalizes from the nucleolus to the viral replication compartments (VRC) upon infection with herpes simplex virus type 1 (HSV-1) (Callé et al., 2008; Lymberopoulos and Pearson, 2007; Greco et al., 2012) and other stresses (Jia et al., 2017; Daniely and Borowiec, 2000). NCL is a multifunctional factor implicated in virtually all stages of ribosome biogenesis (Ginisty et al., 1999; Srivastava and Pollard, 1999), requiring its dynamic shuttling between the nucleolus and the nucleoplasm (Chen and Huang, 2001). Other nucleolar proteins whose distribution is sensitive to stress include FBL, UBF1, and NPM1 (Galibert et al., 2001; Yang et al., 2016; Yao et al., 2010). UBF1 is a transcription factor that binds specifically to the rDNA promoters and maintains the active state of rDNA (Roussel et al., 1993; Tuan et al., 1999; Sanij and Hannan, 2009; Sanij et

al., 2008). FBL is a snoRNA-guided methyltransferase responsible for rRNA 2'-O methylation and a pre-rRNA-processing factor essential for the initial steps of ribosomal biogenesis (Lafontaine and Tollervey, 2000; Omer et al., 2002; Tollervey et al., 1993). In addition, FBL binds to nascent transcripts, helping their transition from the FC/DFC interphase to the DFC, where they undergo initial maturation (Lafontaine, 2019). NPM1 assists in ribosome assembly, chromatin modeling, and cell homeostasis (Lindström, 2011). NPM1 is a pentameric protein that mediates the assembly of the GC via heterotypic interactions with nucleolar proteins and rRNA and homotypic interactions with intrinsically disordered regions of nucleolar proteins (Mitrea et al., 2016, 2018). Ki-67 is a "chromosome surfactant" protein located in the nucleoli in interphase cells and the mitotic chromosome periphery in mitotic cells (Verheijen et al., 1989; Kill, 1996). During the interphase, Ki-67 has a specific role in the organization of heterochromatin (Sun and Kaufman, 2018; Sobecki et al., 2016; Stenström et al., 2020); during mitosis, it is essential to reassemble the nucleolus (Lafontaine et al., 2021; Stenström et al., 2020).

Autonomous parvoviruses have non-enveloped icosahedral particles of ~25 nm in diameter, enclosing a linear single-stranded DNA genome of ~5.0 kb. A typical parvovirus genome contains two open reading frames that encode several structural and non-structural proteins (Cotmore et al., 1983). The canine parvovirus (CPV) capsid is composed of the structural viral proteins VP1 and VP2, with the latter also being N-terminally cleaved into a third structural protein, VP3, in mature virions (Weichert et al., 1998). CPV and other protoparvoviruses encode two non-structural proteins, NS1 and NS2 (Cotmore et al., 1983). The CPV NS1 protein is a multifunctional protein that exhibits site-specific DNA binding, ATPase, helicase, and nickase activities (Niskanen et al., 2010, 2013). NS1 localizes into the nuclear VRC distributed throughout the nucleus but is absent from the nucleolar region (Ihalainen et al., 2009). NS2 of

another protoparvovirus, the minute virus of mice, has been linked to viral DNA replication, translation of viral mRNA, capsid assembly, and pre-lytic nuclear egress (Cotmore et al., 1997; Naeger et al., 1990; Eichwald et al., 2002). Although the function of CPV NS2 is currently mostly undefined, our recent studies have revealed a potential role in chromatin remodeling and DNA damage response during replication (Mattola et al., 2022b).

Here, we investigated how CPV infection impacts nucleolar morphology and function. We show that infection leads to the redistribution of key nucleolar proteins and rRNA, extensive remodeling of nucleolar structure, and reorganization of nucleolus-associated chromatin. Notably, these alterations are accompanied by marked changes in pre-rRNA processing, highlighting the profound effects of CPV on nucleolar homeostasis.

Results

Nucleolar structure is remodeled during infection

To test if viral infection impacts nucleolus homeostasis and ribosome biogenesis, we analyzed the distribution of critical nucleolar proteins and rRNA in CPV-permissive Norden Laboratory Feline Kidney (NLFK) cells. We examined the distribution of representative markers of the major nucleolar compartments. We used UBF1, FBL, NCL, NPM1, and Ki-67 antibodies to label FC, DFC, PDFC, GC, and NR, respectively (**Fig. 1 a**). NS1 detection was used as a proxy to follow the progression of CPV infection.

At 24 hours post infection (hpi), UBF1 and FBL were relocalized outside of the nucleolar region forming small, punctate foci scattered throughout the nucleoplasmic space while retaining some residual localization in the nucleolus. The emergence of small viral NS1-positive foci, visible at 8 hours post-infection (hpi), initiated the formation of the VRC (**Fig.**

S1). The expansion and coalescence of these foci eventually resulted in an enlarged VRC filling the entire nucleoplasm (**Fig. 1 b and c, Fig. S1 and S2**). Mean volume analysis confirmed that the average size of UBF1 and FBL foci within the nuclear area decreased as the infection progressed up to 24 hpi (**Fig. 1 d**). This was accompanied by a reduction in the fraction of nuclear UBF1 and FBL signal detected in these foci (**Fig. 1 e**), favoring a more diffuse staining pattern. Remarkably, the behavior of PDFC and GC proteins was distinctly different. NCL and NPM1 retained their association with nucleoli during the progression of infection. However, the roundness of NCL and NPM1 regions increased at late infection, indicating a change in phase behavior (**Fig. 1 f and g, Fig. S3 a and S4**). The measurement of NCL-stained regions suggested that the volume of the nucleoli remained unchanged in infection (**Fig. S3 b)**. Finally, Ki-67 representing the NR regions was relocalized from the nucleoli into foci scattered throughout the nucleoplasm in infected cells **(Fig. 1 h and i).** The infection led to a partial Ki-67 redistribution from the nucleoli to the nucleoplasm at 8 hpi. At 12 hpi, Ki-67 was seen in the nucleoli and nucleoplasm, accumulating close to the NE, which likely correlates with the reorganization of the host cell chromatin close to the nuclear envelope as the infection progresses **(Fig. S5, and** see also below **Fig. 3 a**). Later, at 24 hpi, Ki-67 showed a homogenous nuclear distribution with a few distinct small foci **(Fig. S5)**.

Quantitative 3D image analysis demonstrated that the volume of rRNA-containing nucleolar regions decreased (**Fig. 2 a and b**). At the same time, the nucleolar intensity of rRNA remained unchanged at late infection compared to control cells (**Fig. 2 c**). Importantly, similar to the observations with the NCL and NMP1 (**Fig. 1 f and g, Fig. S3 a and S4**), rRNA-containing nucleolar regions became increasingly circular in late infection at 24 hpi (**Fig. 2 d**).

In conclusion, upon viral infection, the nucleolus appears to disassemble, starting from its inner core (FC and DFC), which loses integrity, while the more peripheral layers (PDFC and GC) remain somewhat organized but exhibit increased circularity. The NR, which lines the exterior of the nucleolus, is also lost.

Reorganization of nucleolar ultrastructure upon infection

Host chromatin displacement and marginalization near the nuclear envelope (NE) is observed at the late stages of parvovirus infection as the VRC expands (Ihalainen et al., 2009). Little is known about how the infection and infection-induced redistribution of chromatin affect the organization of nucleolus-associated chromatin.

We used ten-fold robust expansion microscopy (TREx) to examine nucleolar chromatin organization and overall protein distribution. TREx enables super-resolution imaging, approaching 25-30 nm resolution, using a conventional confocal microscope by embedding immunostained cell samples in a swellable hydrogel (Damstra et al., 2022). Labeling total protein with a fluorescent NHS ester dye reveals the nanoscale organization and protein intensity within nucleoli, while DAPI staining highlights chromatin distribution (**Fig. 3 a**) (Sheard et al., 2023).

The NHS ester labeling revealed protein accumulation in spherical, nucleolus-like regions within the central nuclear areas of both noninfected and infected NLFK cells at 24 hpi. Immunostaining for FBL showed that, in noninfected cells, FBL localized to protein-dense areas – likely corresponding to DFCs – as expected for typical nucleolar architecture (**Fig. 3 a**). Consistent with earlier observations (**Fig. 1 c and e**), TREx microscopy at 24 hpi confirmed partial redistribution of FBL into nucleoplasmic foci upon infection (**Fig. 3 a**), in agreement

with disassembly of the FCs and DFCs, previously inferred from the nucleolar release of UBF1 and FBL (**Fig. 2 a**).

Analysis of DNA and total protein distribution revealed that in both noninfected and infected cells, chromatin remained condensed near the nuclear envelope and partially around nucleoli (**Fig. 3 a and b**). However, perinucleolar chromatin intensity was markedly higher in infected cells, coinciding with reduced protein signal in these chromatin-dense zones (**Fig. 3 a and c**). In contrast, regions just inside the nucleolar border showed increased protein intensity during infection (**Fig. 3 c**). The infection also led to a more irregular distribution of DNA within nucleoli, with the formation of large intra-nucleolar DNA foci and increased variability compared to noninfected cells (**Fig. 3 a, d)**. These foci coincided with areas of low protein density and were often surrounded by FBL, yet did not overlap with condensed perinucleolar DNA (**Fig. 3 a,** white arrowhead at 24 hpi). This pattern suggests that the infection drives DNA accumulation in nucleolar interstices, as previously identified by EM studies (Thiry, 1993; Thiry and Lafontaine, 2005; Lafontaine et al., 2021). Finally, infection also disrupted the spatial relationship between DNA and protein: whereas DNA and total protein signals were largely anti-correlated in noninfected cells, they became positively correlated upon infection (**Fig. 3 d, e**).

The 3D reconstructions of TREx data demonstrated that the low-intensity protein regions formed interconnected channel networks, which sometimes spread throughout the nucleoli in noninfected and infected cells. In infected cells, the channels formed larger spherical vacuolar cavities, which were also interconnected. Notably, a substantial part of channels in noninfected and infected cells were DNA-containing interstices, or DNA was located close to the channels (**Fig. 3 f and movie M1**).

To further examine the infection-induced changes in the 3D structure of nucleoli, NLFK cells were grown and infected on electron microscopy (EM) grids and analyzed using cryo soft X-ray tomography (cryo-SXT). Cryo-SXT allows label-free imaging of carbon- and nitrogen-containing cellular structures while preserving cells in a near-native frozen state and, as shown here, is particularly efficient in distinguishing normal and diseased-state nucleoli. The attenuation of soft X-rays into intracellular structures creates biomolecule concentration- and composition-dependent images (Loconte et al., 2022; Harkiolaki et al., 2018) from which quantitative features relevant to the material state of biomolecular condensates can be extracted. Notably, measurements of the linear absorption coefficient (LAC) provide a method to characterize nucleolar thickness and the distribution of low- and high-density regions of the nucleolus.

Cryo-SXT images and cross-sections of 3D cryo-SXT reconstruction data revealed misshaped nucleoli with an increased number of low-density foci at 24 hpi compared to noninfected cells (**Fig. 4 a and b, movie M2**). The 3D analysis of the SXT data indicated that the roughness and the total LAC value of nucleoli (**Fig. 4 c and d**) remained unchanged in infection. However, the nucleolar structure became heterogeneous with the increased appearance of infection-induced low-density foci (**Fig. 4 a** and **b**). These foci are reminiscent of the low-protein density interstices observed using TREx (**Fig. 3 a**). The number and total volume of these low-density foci increased during infection (**Fig. 4 e and f**). Sometimes, individual foci formed thin, low-density connections extending from the nucleolar rim towards the center of the nucleoli, as seen in noninfected cells (**Fig. 4 a and b**). In our TREx studies, similar structures were observed to contain intranucleolar chromatin (**Fig. 3 a and f**). Cryo-SXT analysis also revealed

that the number of low-density regions was higher in infected than in noninfected cell nucleoli (**Fig. 4 g**).

In conclusion, the high-resolution analysis of intranucleolar DNA and total protein content by expansion microscopy and cryo-SXT revealed the ultrastructural reorganization of nucleolar DNA and proteins, as well as the emergence of enlarged DNA-containing channels and low-density foci during infection.

NS2 interacts with host cell proteins involved in nucleolar organization and rRNA processing

Our previous findings revealed that CPV NS2 localizes to the nucleolus during the infection and that this protein may interact with nucleolar proteins (Mattola et al., 2022b). To further investigate the extent of NS2 association with nucleolar proteins, we analyzed in greater detail our previously established NS2 interactome (Mattola et al., 2022b), now focusing on the nucleolus. Our NS2 interactome was generated by proximity-dependent biotin identification (BioID) assays (Liu et al., 2018), and mass spectrometry analyses of NS2-associated proteins. Specifically, our dataset was produced using a BirA*-tagged NS2 fusion protein expressed in Flp-In T-Rex 293 cells infected with CPV (24 hpi) and, as control, in noninfected cells.

The analysis of NS2-associated nucleolar proteins indicated that the number of proteins was slightly higher in noninfected cells (33 proteins) than in infected cells (27) (spectral count ≥ 2; Bayesian false discovery rate, BFDR, cutoff of <0.01 or <0.05) (**Fig. 5 a and b, Table T1 and T2)**. The NS2-associated proteins in noninfected cells represent putative interactions of NS2 independent of infection. In infected cells, most NS2-associated proteins with various biological functions were localized in the GC subcompartment of the nucleolus (20/27 of all

spectral counts). Putative NS2 interactors were also located in the FC and DFC (six counts ≥ 2) and in the NR (seven counts ≥ 2), and some proteins showed dual localization (six) (**Fig. 5 c, Table T1 and T2)**. The highest-ranked high-confidence interactor detected by BioID was Ki-67 (MKI67), which was found in interaction with NS2 in both noninfected and infected cells (BFDR/spectral count 0.02/78.5 in infected and 0.04/76.5 in noninfected cells) (**Fig 5 a and b**, **Table T1 and T2).**

To confirm the association between Ki-67 and NS2, we used a Proximity Ligation Assay (PLA) which generates discrete fluorescent foci at sites of interactions detectable by light microscopy only when the two antigens are within 40 nm of each other (Söderberg et al., 2006). In noninfected cells, only few foci per nucleus were detected (**Fig. 5 d**). The number of foci in infected cells increased sharply, exhibiting a highly distinctive perinuclear distribution pattern, nearly perfectly concentric. Most punctate nuclear PLA signals were localized in the nucleoplasm near the NE (**Fig. 5 d and e),** where chromatin accumulates (**Fig. 3 a**). Most of the signals were accumulated in peripheral areas, not in the center of the nucleus (**Fig. 5f)**. The negative NS2 and Ki-67 control in non-infected cells and technical probe controls (**Fig. 5 d and e, Fig. S6)** indicated that the background in the nuclear area was low.

Gene Ontology (GO) annotation analyses of biological processes indicated that 12 putative interaction partners of NS2 are involved in the organization of the nucleolus (GO:0007000, three proteins) and in rRNA processing (GO:0006364, nine proteins) (**Fig. 6 a, Table T1 and T2**). The nine proteins grouped by their involvement in rRNA processing included three DEAD-box helicases: DDX27, DDX54, and DDX56. DDX27 (BFDR <0.01) is essential for rRNA synthesis, processing, and early ribosomal assembly, and it colocalizes with FBL in the DFC region (Kellner et al., 2015; Bennett et al., 2018). We investigated if the infection affects

the subcellular distribution of three NS2-associated proteins: DDX27, Epstein-Barr virus nuclear antigen 1 binding protein 2 (EBNA1BP2), and the nucleolar protein interacting with the FHA domain of Ki-67 (NIFK). In infected cells, DDX27 labeling retained the nucleolar localization but was additionally accumulated in the nucleoplasm, showing increased nuclear intensity (**Fig. 6 b and c**). EBNA1BP2 (BFDR <0.05) is an NPM1-binding protein involved in ribosomal subunit assembly (Uchihara et al., 2021; Huber et al., 2000; Kim et al., 2020). EBNA1BP2 was detected in the nucleolar area with decreased nuclear intensity in infected cells (**Fig. 6 d and e**). NIFK, the nucleolar protein interacting with the FHA domain of Ki-67 (BFDR <0.01), is an interactor of Ki-67 and NPM1 and participates in rRNA maturation colocalizing with FBL in the DFC area (Takagi et al., 2001; Sun and Kaufman, 2018; Mattola et al., 2022b; Pan et al., 2015). Upon infection, NIFK is concentrated in the nucleolar area (**Fig. 6 f and g**).

In conclusion, we detected several NS2-associated nucleolar proteins, including ribosome biogenesis factors, and showed for several of them that their association with the nucleolus is affected upon infection.

Pre-rRNA processing is affected during CPV infection

To monitor how CPV infection may affect pre-rRNA processing, we analyzed rRNA intermediates using northern blotting in infected NLFK cells at 8, 12, and 24 hpi and, as a control, in noninfected cells (**Fig. 7**, **Fig. S7**). The pre-rRNA processing pathway has not been described in felines, so we started by designing a set of probes specific to feline pre-rRNAs, targeting all four non-coding spacers (**Fig. 7 a**). We used the rDNA of the *Felis catus* (domestic cat) genome as a reference (see Materials and methods). We modeled the feline pre-rRNA

processing pathway on the well-characterized mouse one (Mullineux and Lafontaine, 2012), a closely related vertebrate.

The most striking effects observed upon infection were: 1) a transient increase of several pre-rRNA species, observed at 8 and 12 hpi (these include the species 45S/47S, 36S, 32S, 18S-E, 12S, and species "e"), and 2) a decrease of others (notably of the 20S and "b") (**Fig. 7 b**, and, for quantification, see heat maps on **Fig.** 7 **c**). Such effects are consistent with inhibition of pre-rRNA processing at multiple cleavages leading to a slowdown in ribosome production during viral infection (See Discussion).

These alterations of the steady-state levels of pre-rRNAs were perfectly reproducible, as shown by analysis in four independent biological replicates (**Fig. S7**). Interestingly, a return to near normal pre-rRNA levels was observed at the latest time point of infection inspected, 24 hpi (e.g., compare levels of 47S/45S, 36S, or 12S in the NI and 24 hpi samples). Such recovery at a late stage of infection indicates that the inhibitions caused by the presence of the virus in cells are transient in nature. Nonetheless, at this late time point post infection, the levels of 41S are strikingly higher than in noninfected cells, indicating some persistent effects of infection on pre-rRNA processing (**Fig. 7 c and d, Table T3**).

In conclusion, CPV infection of cells is accompanied by a transient yet substantial inhibition of pre-rRNA processing at multiple cleavage steps, leading to an unbalanced production of pre-rRNA precursors.

Discussion

A key feature of viruses is their ability to redirect cellular resources for their benefit, hijacking essential pathways and molecular nanomachines such as the ribosome. The nucleolus, the cell's ribosome factory and central hub of energy consumption, is also a frequent target (Thoms et al., 2020). The nucleolus is rich in diverse catalytic activities, including folding, modification, and cleavage. Many DNA viruses, such as HSV-1, adenovirus, and AAV, are known to target the nucleolus to interfere with host cell function and to direct its proteins there to facilitate viral replication (Matthews et al., 2011; Callé et al., 2008; Salvetti and Greco, 2014; Lee et al., 2003; Wistuba et al., 1997). However, how autonomous parvovirus infection may impact nucleolar events has remained largely unknown. Our findings demonstrated that CPV infection can induce profound structural alterations of the nucleolar organization (**Figs. 1-4**) and transient alterations of pre-rRNA processing (**Fig. 7**).

Infection impacts the distribution of nucleolar proteins and chromatin

Viral infection has been reported to lead to striking changes in the nucleolar architecture and the redistribution of nucleolar proteins (Greco, 2009; Hiscox, 2007; Atari et al., 2022; Salvetti and Greco, 2014). In HSV-1 infection, nucleolar UBF1 is relocalized from the FC to the VRC area, where it plays a role in viral replication (Stow et al., 2009). In Kaposi's sarcoma-associated herpesvirus (KSHV), FBL is released into the nucleoplasm (Atari et al., 2022). The methyltransferase activity of FBL is also essential for cytoplasmic replication of several pathogenic viruses such as measles, mumps, and respiratory syncytial viruses (Deffrasnes et al., 2016). In HSV-1 and cytomegalovirus infections, both NCL and NPM1 become dispersed into the nucleoplasm (Callé et al., 2008; Lymberopoulos and Pearson, 2007, 2010; Bender et al., 2014; Greco et al., 2012). NPM1 is removed from the nucleoli by the endonuclease function of the HSV-1 endonuclease UL24 (Callé et al., 2008; Lymberopoulos et al., 2011). Both

cellular NCL and viral UL24 are essential for the nuclear egress of HSV-1 capsids (Sagou et al., 2010; Callé et al., 2008; Lymberopoulos et al., 2011). This suggests a link between the HSV-1 infection-induced disruption of nucleolar structure integrity and viral egress.

This study focused on CPV infection and its impact on nucleolar architecture. Our findings show that the FC/DFC and NR substructures are disassembled during infection, leading to the partial release of nucleolar marker proteins into the nucleoplasm. Remarkably, during the natural disassembly of the nucleolus at the onset of mitosis in cycling cells, the FC and DFC are also the first subphases to disappear (Lafontaine et al., 2021), highlighting a parallel between nucleolar breakdown during mitosis and that induced by CPV infection. These results are consistent with our previous work, showing that CPV infection causes cell cycle arrest at the G2/M checkpoint, interfering with its release and the progression into early mitotic events (Mattola et al., 2022a).

In the nucleoplasm, the nucleolar proteins overlap with the enlarged VRC region, filling the entire nucleoplasm at the late stages of infection (**Fig. 1**). Remarkably, the PDFC and GC, markers (NCL, and NPM1, respectively) remained associated with the nucleolar area, forming protein-rich centers with increased circularity in late infection. Interestingly, NCL has earlier been shown to form complexes with the viral single-stranded genomes of MVM in vitro (Barrijal et al., 1992) and to bind AAV-2 capsids assembled in the nucleoli in vivo (Qiu and Brown, 1999; Wistuba et al., 1997; Johnson and Samulski, 2009). Our findings show that the inner core of the nucleolus and the NR lose integrity upon CPV infection, whereas the peripheral layers remain relatively intact. This suggests that in contrast to HSV-1 infection, CPV infection induces only a partial disruption of nucleolar integrity. However, the increased circularity of the nucleolar condensates containing NCL, NPM1, and pre-rRNAs indicates an

alteration of surface tension of these foci and a change in phase behavior (**Fig. 2**). These findings suggest that parvovirus infection changes nucleolar organization with consequences on ribosome biogenesis.

The probing of nucleolar ultrastructure by TREx and cryo-SXT revealed that the progression of infection leads to extensive structural remodeling of nucleoli, including condensation of chromatin around the nucleoli. The observation using TREx microscopy showed that the infection also resulted in the emergence of enlarged nucleolar low-protein density interstices and their vacuolar cavities (**Fig. 3 and 4**). Similar structural changes have been observed in stressed cells after vitamin C and K3 (Apatone) and actinomycin D treatments (Jamison et al., 2010; Tchelidze et al., 2017). The emergence of interconnected channels forming a network is compatible with the notion that the nucleolus has been described as a percolated biomolecular condensate. It is interesting to observe that the size and distribution of the internal cavities seem to change drastically, becoming larger upon viral infection as the nucleolus is remodeled. The virus-induced compaction of intranucleolar DNA could limit chromatin accessibility to transcription factors and thereby downregulate the level of rRNA gene transcription. The redistribution of nucleolar UBF1, a regulator of transcription of rDNA (Sanij and Hannan, 2009; Sanij et al., 2008), along with chromatin reorganization, may reduce rRNA transcription. However, our findings show that the total intensity of nucleolar rRNA and the production of primary rRNA transcripts remain relatively unchanged in infection. This may suggest that the partial compaction of intranucleolar chromatin in infected cells does not necessarily lead to significant interference with rRNA transcription. However, the infection may impact the pre-rRNA processing pathway.

CPV NS2 interacts with nucleolar proteins

During the infection of various viruses, several proteins localize to the nucleolus, where they interact with nucleolar proteins (Salvetti and Greco, 2014; Iarovaia et al., 2021). These interactions lead to the virus-induced disruption of nucleolar function and recruitment of cellular proteins to aid viral replication. During henipavirus infection (RNA virus family *Paramyxoviridae*), the viral matrix proteins interact with Treacle, a nucleolar protein that regulates rDNA transcription (Rawlinson et al., 2018). The acquisition of Treacle during evolution is suggested to coincide with the emergence of the FC subcompartment of the nucleolus (Lafontaine, 2023b; Jaberi-Lashkari et al., 2023). In HSV-1 infection, NPM1 translocation outside of the nucleolus is assisted by the viral protein UL24, and that of NCL by viral ICP4 and US11 (Callé et al., 2008; Lymberopoulos et al., 2011; Greco et al., 2012). The Epstein-Barr virus protein EBNA11 recruits NPM1 for transcriptional activation of its latency genes (Malik-Soni and Frappier, 2014).

Detailed analysis of CPV NS2 interactome (Mattola et al., 2022b) suggested that NS2 interacts with several proteins of the nucleolar inner core, peripheral layers, and NR (**Fig. 5**, and Mattola et al. 2022). These putative nucleolar interactors of NS2 are involved in nucleolar organization and rRNA processing. A major NS2 interactor is the chromosome surfactant protein Ki-67, a protein involved in the organization of heterochromatin in actively dividing mammalian cells (Sobecki et al., 2016; van Schaik et al., 2022; Booth et al., 2014). It also has a role in the nucleolar assembly and organization of perinucleolar chromatin at the NR (van Schaik et al., 2022; Remnant et al., 2021). NS2 was also associated with cellular proteins involved in ribosome biogenesis and rRNA processing, whose subcellular distribution was modified upon CPV infection (**Fig. 6**). The interaction of NS2 with proteins regulating nucleolar organization suggests that NS2 has a role in the profound alteration of nucleolar morphology and function.

CPV infection impacts pre-rRNA processing

Nucleolar structure alterations during CPV infection impacted the function of the nucleolus (**Fig. 7**). There was a transient change in the steady-state levels of most pre-rRNA precursors, which is compatible with the inhibition of cleavage at multiple processing steps. Interestingly, the observed effects on processing appeared transient at 8 and 12 hpi but not later. Remarkably, the steady-state levels of most pre-rRNA returned to near normal levels at 24 hpi at a time of infection when the nucleolar structure was still profoundly impacted.

Why might it be interesting for the virus to repress host cell ribosome biogenesis during infection? Firstly, it is essential to consider that ribosomes are long-lived (i.e., several days) ribonucleoprotein particles that are robustly packaged during assembly. This implies that pre-existing ribosomes remain available to produce the viral components throughout infection. Secondly, ribosome biogenesis is an energy-intensive process that engages most cellular activities, including all three RNA polymerases and hundreds of factors involved in RNA cleavage, modification, folding, and transport – some are also essential for other cellular substrates. Additionally, ribosome biogenesis spans multiple cellular subcompartments: it begins in the nucleolus, continues in the nucleoplasm, and is finalized in the cytoplasm. Thus, it is reasonable to assume that suppressing ribosome biogenesis, at least temporarily, is beneficial for the virus, as it reduces the host cell's energy expenditure and redirects resources toward processes that favor viral replication.

In conclusion, our work demonstrates that autonomous parvoviruses, such as CPV, not only remodel the structural organization of the nucleolus but also modulate its function. This study provides novel insights into the functional and physical interactions between autonomous parvoviruses and the nucleolus.

Materials and methods

Cell lines, plasmids, and viruses

Norden laboratory feline kidney (NLFK) cells were maintained as previously described (Mattola et al., 2022b). Infectious plasmid clone pBI265 (Parrish, 1991) was used to generate CPV-2. Cells were transfected using JetOptimus transfection reagent (Polyplus-transfection, Illkirch, France) as described in the manufacturer's instructions. Virus stocks were produced in NLFK cells and concentrated using an Amicon® Stirred Cell ultrafiltration system (Merck KGaA, Darmstadt, Germany).

Antibodies

The following primary antibodies against viral antigens used in confocal microscopy analyses were generous gifts: mouse anti-NS1 (Dr. Caroline Astell, University of British Columbia, Vancouver, Canada) (Yeung et al., 1991). mouse anti-NS2 and rabbit anti-VP2 (Dr. Colin Parrish, Cornell University, Ithaca, NY, USA) (Wang et al., 1998; Weichert et al., 1998). Commercial primary antibodies against cellular proteins were used according to the manufacturer's instructions: rabbit UBF1 (ab244287, Abcam, Cambridge, UK), rabbit FBL (ab166630, Abcam), rabbit NCL (ab22758, Abcam), mouse NPM1 (conjugated to Alexa647, MA3-25200-A647, Invitrogen, Life Technologies, Waltham, MA), rabbit Ki-67 (ab15580, Abcam), mouse rRNA (MA1-16628, Invitrogen) (Garden et al., 1995), rabbit DDX27 (17087-1-AP, ProteinTech Europe, Manchester, UK), rabbit EBNA1BP2 (PA5-97189, Invitrogen), rabbit NIFK (HPA 035735, Sigma, Merck KGaA). The primary antibodies were followed by goat anti-mouse or anti-rabbit Alexa448, Alexa546, and Alexa647 conjugated secondary antibodies (Thermo Fisher Scientific, Waltham, MA, USA).

Immunolabelling and confocal microscopy

For microscopy sample preparation, NLFK cells were cultured on glass coverslips at 37°C with 5 % CO_2. Cells were infected with CPV and fixed at 8, 12, or 24 hpi in 4% paraformaldehyde for 12 minutes. Following fixation, cells were permeabilized with 0.1% Triton X-100 in phosphate-buffered saline supplemented with 0.1% bovine serum albumin. After primary antibody immunolabeling, cells were labeled with mouse or anti-rabbit secondary fluorescent antibodies. DNA was stained with Pro-Long Diamond anti-fade media with DAPI (Thermo Fisher Scientific).

The microscopy of immunolabeled samples was performed with Leica TCS SP8 FALCON (Leica microsystems, Mannheim, Germany) and Nikon A1R (Nikon, Tokyo, Japan) laser scanning confocal microscopes. The parameters for images acquired with Leica TCS SP8 FALCON were as follows: DAPI was excited with a 405 nm diode laser, and the fluorescence was collected between 415-495 nm. Alexa488 and Alexa546 were excited with 499 nm and 557 nm wavelengths of pulsed white light laser (80 MHz). The emission detection range was adjusted to 505-561 nm for Alexa488 and 568-648 nm for Alexa546. Microscopy images with Nikon were acquired by exciting DAPI with a 405 nm diode laser and collecting with a 450/50 nm band-pass filter. Alexa488 was excited with a 488 nm argon laser, and the fluorescence was collected with a 515/30 nm band-pass filter. Alexa 647 was excited with a 640 nm diode laser and detected with a 660 long-pass filter. The image resolution was 512 x 512 or 1024 x 1024 pixels, with a pixel size between 30-60 nm in the x- and y-directions and 180-300 nm in the z-direction. A fixed optical configuration was used to acquire all images of the same sample set.

The nuclei were segmented from the DAPI stain using Otsu's or minimum cross entropy method (Otsu, 1979; Li and Lee, 1993). Total fluorescence intensities in the nucleus and

nucleoli were calculated by summing the pixel intensity values within the segmented regions. The foci of nucleolar proteins were segmented by adjusting the intensity threshold to 33%, 45%, and 55% of the intensity range in each nucleus for UBF1, fibrillarin, and nucleolin, respectively. rRNA signal was segmented using Otsu's algorithm. The intensity distributions of labels with respect to the nuclear or nucleolar border were determined by calculating the shortest distance of each pixel to the border and calculating mean intensity as a function of the distance using 2-pixel wide distance bins for averaging. Due to the flat shape of fixed cells, the confocal section with the largest nuclear area was selected for the analyses of intensity with respect to the nuclear border, and 2D Euclidean distance was used as a metric. Since there can be many nucleoli in one cell and the nucleoli can lie on various confocal planes, the whole 3D stack was used in the analyses for the nucleolar border, and 3D Euclidean distance was used as a metric. Correlations between DNA staining and antibody labels were determined by using Pearson correlation coefficients in the nuclear region. For all the analyses, the given statistics were calculated over cells. The circularity of the single planes of segmented rRNA antibody-labeled nucleoli was determined with Fiji (Schindelin et al., 2012). Circularity determination in Fiji is based on the equation 4pi(area/perimeter^2), where a perfect circle is indicated by the value 1.0.

Ten-fold robust Expansion Microscopy and visualization

NLFK cells were grown on coverslips as previously. Noninfected and infected cells were fixed at 24 hpi in 4% PFA (Electron Microscopy Sciences, SKU 15710, diluted to 4% with sterile PBS) for 12 min at room temperature, after which the cells were permeabilized with 0.5% Triton X-100 in PBS supplemented with 0.5% bovine serum albumin (BSA). The permeabilized cells were immunolabelled with mouse anti-NS1 and rabbit anti-fibrillarin primary antibodies, and anti-mouse Alexa546 and anti-rabbit Alexa448 secondary antibodies.

Primary and secondary antibodies were used at 3-fold and 4-fold higher concentrations, respectively, compared to standard immunolabeling.

Ten-fold Robust Expansion Microscopy was performed according to the protocol described earlier (Damstra et al., 2022). Briefly, immunolabeled samples on glass coverslips were anchored using 0.1 mg/ml Acrolyl-X (Invitrogen, Catalog number A20770) overnight at + 4°C. Gelation was performed with a gel containing 14.2% acrylamide (Sigma-Aldrich, product number A9099), 10.1% sodium acrylate (AmBeed, catalog number A107105), 0.005% bis-acrylamide (Sigma-Aldrich, product number M1533), 0.15% ammonium persulfate (Sigma-Aldrich, A3678), and 0.15% TEMED (Sigma-Aldrich, product number T22500) in PBS for 1 hour at 37 °C. After gelation, the samples were denatured in 0.2 M NaCl, 50 mM Tris (pH 6.8), and 5.76% SDS for 1.5 hours at 78°C and washed twice with PBS. Gels were stained for the total protein with 20 µg/ml of ATTO 647N NHS (Atto-tec, Siegen Germany) dye in sodium bicarbonate buffer (Sigma) for 1 hour at RT. DAPI (Roche) diluted 1:6000 in PBS was used to stain DNA for 60 minutes before the expansion. Gels were expanded in distilled H_2O, changing the water until no further expansion was observed. The achieved expansion factor (approximately 7.5) was calculated by comparing the gel size after the gelation and after the expansion and back-calculated into image scale bars.

Images of expansion samples were acquired with a Leica SP8 confocal microscope using the 63x water immersion objective (1.2 NA). DAPI was excited with a 405 nm laser and detected with a PMT detector at 412-480 nm. Alexa 488 was excited with a 499 nm laser and detected at 506-552 nm using a Leica HyD SMD detector. Alexa 546 was excited with a 557 nm laser and detected at 566-611 nm using a Leica HyD SMD detector. The total protein stain was excited with a 645 nm laser and detected at 652-800 nm using a Leica HyD SMD detector. The

pixel size was 90 nm in the x- and y-directions and 356 nm in the z-direction. The images were first denoised using a Gaussian filter with a radius of three pixels to analyze the DNA and total protein labels in the nucleoli. Then, the nucleoli were segmented by setting an intensity threshold for the total protein channel using Otsu's algorithm (Otsu, 1979). In segmenting cells with contiguous nucleoli and strong total protein signal at the nuclear envelope, the total protein images were manually edited to remove the continuity and prevent the segmentation of other regions besides the nucleoli. The coefficient of variation (the standard deviation divided by the mean) for the DNA and total protein labels and the Pearson correlation coefficient were calculated for the pixels belonging to the segmented nucleolar region. The intensity of the labels for the nucleolar border was analyzed by calculating the minimum distance of each pixel to this border, grouping the pixels based on their distance to the border, and calculating the mean intensity of each group. Surface renderings of the noninfected and infected nucleoli were created with Dragonfly 3D World v2024.1.

Cryo-SXT of adherent cells on grids

NLFK cells were grown and infected with CPV for 24 hours at 37°C on Au grids (Quantifoil-coated Au-TEM finder grids, R2/2, G200F1, Gilder, Jena, GER). Noninfected and infected cells were fixed with 4% PFA for 12 minutes at room temperature and labeled with 1µg/ml Hoechst 33342. The infected cells were identified by an infection-induced chromatin marginalization using a widefield microscope (Leica DM IL LED, Leica Microsystems GmbH, Germany) with HC FL PLAN 40X/0.65NA air objective or a confocal microscope (Leica SP 8, Leica Microsystems GmbH, Germany) with HC PL APO 63x/1.2NA water immersion objective. The grids were plunged into liquid ethane for vitrification (Leica EM GP2, Leica Microsystems GmbH, Germany) and kept at -196°C until imaging. Using a compact soft X-ray microscope, the pre-vitrification-located infected cells were re-located by a low

magnification SXT imaging, and a built-in cryo-fluorescence microscopy from the vitrified grids, and tomographic tilt-series of infected cells were collected (SXT100, Sirius XT, Dublin, IRE, https://siriusxt.com/) (O'Connor et al., 2024; Fahy et al., 2021). The tilt series were acquired assets of X-ray projections covering a 120° tilt range with one-degree increments. The exposure per projection ranged from 15 to 60 seconds, depending on the sample ice thickness and tilt angle. The exposure time was increased to 120 seconds at high tilt angles for samples with particularly thick ice. The samples were maintained at temperatures of -163°C or lower throughout all experimental stages. The tomographic data alignment and data analysis were done as described in detail (Leclerc et al., 2024).

BioID analyses

BioID of CPV NS2 protein was performed as previously described (Mattola et al., 2022b). Briefly, a biotin protein ligase was fused to NS2 to allow for the detection of proximal and interacting proteins by biotin tags. The high-confidence NS2 interactions identified among the biotinylated proteins were further screened for nucleolar interactors. Data was analyzed with SAINTexpress (Teo et al., 2014), and filtered using a protein-level Bayesian FDR of 0.05 as the cutoff. Controls included four different GFP-BirA* constructs, including NLS-GFP. Further filtering was done by integrating control experiment data from the CRAPome contaminant repository (Mellacheruvu et al., 2013). The high-confidence interactor set was used for Protein ANalysis THrough Evolutionary Relationships (PANTHER) classification system (http://www.pantherdb.org/) to create GO biological process annotation chart of NS2 interactors (**Table T1**).

Proximity ligation assay (PLA)

The association of NS2 with the key interactor Ki-67 during infection was verified with PLA. NLFK cells were grown on coverslips and infected with CPV. Infected and noninfected samples were fixed at 24 hpi in 4% formaldehyde for 12 min and permeabilized using 0.1% Triton X-100 in PBS. NS2 and Ki-67 were identified with mouse anti-NS2 and rabbit anti-Ki-67 antibodies, respectively, and the assay was performed using the Duolink In Situ Orange Mouse/Rabbit kit (Merck KGaA) following the manufacturer's protocol. Technical controls were prepared from infected samples by omitting the anti-NS2 antibody or by omitting the PLA probes. Samples were embedded into a non-hardening mounting medium containing DAPI and imaged with a Nikon A1R confocal microscope with Plan Apo VC 60x oil immersion objective (NA 1.4). The human-in-the-loop machine-learning-based characterization of DAPI-labeled chromatin distribution verified the infection in PLA-labeled cells. The machine learning model was built, trained, and tested using Keras 1.0 with TensorFlow 2.0 backend using Python 3.9 in the Google Colab pro-environment. The deep learning code and model developed in this study can be found at https://github.com/leclercsimon74/Infection_Prediction_CPV. DAPI was excited with a 405 nm diode laser, and the fluorescence was collected with a 450/50 nm band-pass filter. PLA signals were excited with a 561 nm sapphire laser, and the fluorescence was collected with a 595/50 nm band-pass filter. Single cells were imaged as stacks (resolution 512 x 512 pixels, pixel size in xy 60 nm, z sampling distance 200 nm).

DAPI signal was used to segment the nuclei from image stacks by automatic minimum cross entropy segmentation (Li and Lee, 1993) and filling any holes within the segmented regions. The PLA signals were segmented using the maximum entropy algorithm (Kapur et al., 1985), and their geometric centers were determined. The number of PLA signals with their geometric center located within the segmented nucleus was counted.

Quantitative northern blotting analysis of pre-rRNA

Total RNA was extracted from noninfected and infected NLFK cells at 8, 12, and 24 hpi with TRI reagent solution (Thermofisher), according to the manufacturer's instructions. To analyze high-molecular-weight RNAs, 5 µg total RNA was resolved in a 1.2% formaldehyde-agarose denaturing gel, followed by electrophoresis at 65 V. Agarose gels were transferred overnight by capillarity onto Hybond-N+ membranes (Cytiva) in 10x saline sodium citrate (SSC). Membranes were prehybridized at 65°C for 1 h in a solution containing 50% formamide, 5x SSPE, 5x Denhardt's solution, 1% (wt/vol) SDS, and 200 mg/ml fish sperm DNA (Roche). Hybridization with specific ^{32}P-labeled oligonucleotide probes was carried out for 1 h at 65°C and overnight at 37°C. Probe sequences are listed in Table S1. The membranes were washed and exposed to Fuji imaging plates (Fujifilm). Signals were captured with a Phosphorimager (FLA-7000, Fujifilm) and quantified with Multi Gauge Software (Fujifilm, v 3.1).

Probe sequence Table

The probes LD4838, LD4804, LD4806, and LD4891 were designed using the Felis catus_Fca126_mat1.0 genome (NCBI RefSeq assembly: GCF_018350175.1). Their sequence is given in **Table S1**.

Table S1: Probes used in this work.

Probe	Sequence
LD4838	5' ACGAAGCCTTGCGAGGGTGGGTTT 3'
LD4804	5' CGACCGCTGCGCTCTCTCGTTAAT 3'
LD4806	5' CCGTCGTCTGCACTTAGGGGGACG 3'
LD4891	5' GCGAGAGGCGACGGGGAAGAATCC 3'

Quantification of pre-rRNA processing intermediates (Supplementary Table 3)

Data availability

All relevant data and supporting information files are in the manuscript.

Contributions

Conceptualization: Vesa Aho, Salla Mattola, Denis Lafontaine, Maija Vihinen-Ranta
Data curation: Salla Mattola, Moona Huttunen, Satu Hakanen, Aynur Soenmez, Sergey Kapishnikov, Visa Ruokolainen, Denis Lafontaine,
Formal analysis: Simon Leclerc, Kari Salokas, Vesa Aho
Funding Acquisition: Colin R Parrish, Lafontaine, Maija Vihinen-Ranta
Investigation: Salla Mattola, Moona Huttunen, Satu Hakanen, Aynur Soenmez, Alessandro Zannotti, Sergey Kapishnikov, Visa Ruokolainen, Kari Salokas
Methodology: Salla Mattola, Simon Leclerc, Kari Salokas, Markku Varjosalo, Kenneth Fahy, Denis Lafontaine
SXT data acquisition: Alessandro Zannotti
Software: Simon Leclerc, Vesa Aho
Resources: Markku Varjosalo, Colin R Parrish, Kenneth Fahy, Denis Lafontaine, Maija Vihinen-Ranta
Project Administration: Maija Vihinen-Ranta
Visualization: Salla Mattola, Moona Huttunen, Satu Hakanen
Writing – Original Draft Preparation: Denis Lafontaine, Maija Vihinen-Ranta
Writing – Review & Editing: Moona Huttunen, Satu Hakanen, Leena Latonen, Vesa Aho, Salla Mattola, Denis Lafontaine, Maija Vihinen-Ranta

The experiments were done using commercially available cell lines without ethical challenges.

Competing interests

The authors have declared that no competing interests exist.

Electronic supplementary material

Supplementary material includes methods, supplementary figures, tables, and movies.

Funding information

This work was financed by the Jane and Aatos Erkko Foundation (MVR), Research Council of Finland under award number 330896 (MVR) and 357490 (LL), European Union's Horizon 2020 research and innovation programme, Compact Cell Imaging Device (CoCID) under

grant agreement No. 101017116 (MVR), the Biocenter Finland, viral gene transfer (MVR), and the Graduate School of the University of Jyvaskyla (SM). The funders had no role in the study design, data collection and analysis, the decision to publish, or the preparation of the manuscript. Research in the Lab of D.L.J.L. was supported by the Belgian Fonds de la Recherche Scientifique (F.R.S./FNRS), EOS [CD-INFLADIS, grant n°40007512], Région Wallonne (SPW EER) Win4SpinOff [RIBOGENESIS], the COST actions EPITRAN (CA16120) and TRANSLACORE (CA21154), the European Joint Programme on Rare Diseases (EJP-RD) RiboEurope and DBAGeneCure.

Acknowledgments

We thank the staff of the Biocenter Finland and Proteomics unit (Helsinki Institute of Life Science, HiLIFE; Institute of Biotechnology Proteomics Unit; Helsinki; Finland) for providing the Bio-ID analysis.

References

Andersen, J.S., Y.W. Lam, A.K.L. Leung, S.-E. Ong, C.E. Lyon, A.I. Lamond, and M. Mann. 2005. Nucleolar proteome dynamics. *Nature*. 433:77–83. doi:10.1038/nature03207.

Anikin, L., and D.G. Pestov. 2022. 9-Aminoacridine Inhibits Ribosome Biogenesis by Targeting Both Transcription and Processing of Ribosomal RNA. *Int J Mol Sci*. 23:1260. doi:10.3390/ijms23031260.

Atari, N., K.S. Rajan, V. Chikne, S. Cohen-Chalamish, T. Doniger, O. Orbaum, A. Jacob, I. Kalt, S. Michaeli, and R. Sarid. 2022. Lytic Reactivation of the Kaposi's Sarcoma-Associated Herpesvirus (KSHV) Is Accompanied by Major Nucleolar Alterations. *Viruses*. 14:1720. doi:10.3390/v14081720.

Barrijal, S., M. Perros, Z. Gu, B.L. Avalosse, P. Belenguer, F. Amalric, and J. Rommelaere. 1992. Nucleolin forms a specific complex with a fragment of the viral (minus) strand of minute virus of mice DNA. *Nucleic Acids Res*. 20:5053–5060. doi:10.1093/nar/20.19.5053.

Bender, B.J., D.M. Coen, and B.L. Strang. 2014. Dynamic and nucleolin-dependent localization of human cytomegalovirus UL84 to the periphery of viral replication compartments and nucleoli. *J Virol*. 88:11738–11747. doi:10.1128/JVI.01889-14.

Bennett, A.H., M.-F. O'Donohue, S.R. Gundry, A.T. Chan, J. Widrick, I. Draper, A. Chakraborty, Y. Zhou, L.I. Zon, P.-E. Gleizes, A.H. Beggs, and V.A. Gupta. 2018. RNA helicase, DDX27 regulates skeletal muscle growth and regeneration by modulation of translational processes. *PLoS Genet*. 14:e1007226. doi:10.1371/journal.pgen.1007226.

Biggiogera, M., K. Bürki, S.H. Kaufmann, J.H. Shaper, N. Gas, F. Amalric, and S. Fakan. 1990. Nucleolar distribution of proteins B23 and nucleolin in mouse preimplantation embryos as visualized by immunoelectron microscopy. *Development*. 110:1263–1270. doi:10.1242/dev.110.4.1263.

Boisvert, F.-M., S. van Koningsbruggen, J. Navascués, and A.I. Lamond. 2007. The multifunctional nucleolus. *Nat Rev Mol Cell Biol*. 8:574–585. doi:10.1038/nrm2184.

Booth, D.G., M. Takagi, L. Sanchez-Pulido, E. Petfalski, G. Vargiu, K. Samejima, N. Imamoto, C.P. Ponting, D. Tollervey, W.C. Earnshaw, and P. Vagnarelli. 2014. Ki-67 is a PP1-interacting protein that organises the mitotic chromosome periphery. *Elife*. 3:e01641. doi:10.7554/eLife.01641.

Boulon, S., B.J. Westman, S. Hutten, F.-M. Boisvert, and A.I. Lamond. 2010. The nucleolus under stress. *Mol Cell*. 40:216–227. doi:10.1016/j.molcel.2010.09.024.

Boyne, J.R., and A. Whitehouse. 2009. Nucleolar disruption impairs Kaposi's sarcoma-associated herpesvirus ORF57-mediated nuclear export of intronless viral mRNAs. *FEBS Lett*. 583:3549–3556. doi:10.1016/j.febslet.2009.10.040.

Callé, A., I. Ugrinova, A.L. Epstein, P. Bouvet, J.-J. Diaz, and A. Greco. 2008. Nucleolin is required for an efficient herpes simplex virus type 1 infection. *J Virol*. 82:4762–4773. doi:10.1128/JVI.00077-08.

Caragine, C.M., S.C. Haley, and A. Zidovska. 2019. Nucleolar dynamics and interactions with nucleoplasm in living cells. *Elife*. 8:e47533. doi:10.7554/eLife.47533.

Chen, D., and S. Huang. 2001. Nucleolar components involved in ribosome biogenesis cycle between the nucleolus and nucleoplasm in interphase cells. *J Cell Biol*. 153:169–176. doi:10.1083/jcb.153.1.169.

Cotmore, S.F., A.M. D'Abramo, L.F. Carbonell, J. Bratton, and P. Tattersall. 1997. The NS2 polypeptide of parvovirus MVM is required for capsid assembly in murine cells. *Virology*. 231:267–280. doi:10.1006/viro.1997.8545.

Cotmore, S.F., L.J. Sturzenbecker, and P. Tattersall. 1983. The autonomous parvovirus MVM encodes two nonstructural proteins in addition to its capsid polypeptides. *Virology*. 129:333–343. doi:10.1016/0042-6822(83)90172-1.

Damstra, H.G.J., B. Mohar, M. Eddison, A. Akhmanova, L.C. Kapitein, and P.W. Tillberg. 2022. Visualizing cellular and tissue ultrastructure using Ten-fold Robust Expansion Microscopy (TREx). *Elife*. 11:e73775. doi:10.7554/eLife.73775.

Daniely, Y., and J.A. Borowiec. 2000. Formation of a complex between nucleolin and replication protein A after cell stress prevents initiation of DNA replication. *J Cell Biol*. 149:799–810. doi:10.1083/jcb.149.4.799.

Deffrasnes, C., G.A. Marsh, C.H. Foo, C.L. Rootes, C.M. Gould, J. Grusovin, P. Monaghan, M.K. Lo, S.M. Tompkins, T.E. Adams, J.W. Lowenthal, K.J. Simpson, C.R. Stewart, A.G.D.

Bean, and L.-F. Wang. 2016. Genome-wide siRNA Screening at Biosafety Level 4 Reveals a Crucial Role for Fibrillarin in Henipavirus Infection. *PLoS Pathog*. 12:e1005478. doi:10.1371/journal.ppat.1005478.

Dubois, M.-L., and F.-M. Boisvert. 2016. The Nucleolus: Structure and Function. *In* The Functional Nucleus. D.P. Bazett-Jones and G. Dellaire, editors. Springer International Publishing, Cham. 29–49.

Eichwald, V., L. Daeffler, M. Klein, J. Rommelaere, and N. Salomé. 2002. The NS2 proteins of parvovirus minute virus of mice are required for efficient nuclear egress of progeny virions in mouse cells. *J Virol*. 76:10307–10319. doi:10.1128/jvi.76.20.10307-10319.2002.

Fahy, K., V. Weinhardt, M. Vihinen-Ranta, N. Fletcher, D. Skoko, E. Pereiro, P. Gastaminza, R. Bartenschlager, D. Scholz, A. Ekman, and T. McEnroe. 2021. Compact Cell Imaging Device (CoCID) provides insights into the cellular origins of viral infections. *J. Phys. Photonics*. 3:031002. doi:10.1088/2515-7647/abfc5a.

Falahati, H., and E. Wieschaus. 2017. Independent active and thermodynamic processes govern the nucleolus assembly in vivo. *Proc Natl Acad Sci U S A*. 114:1335–1340. doi:10.1073/pnas.1615395114.

Feric, M., N. Vaidya, T.S. Harmon, D.M. Mitrea, L. Zhu, T.M. Richardson, R.W. Kriwacki, R.V. Pappu, and C.P. Brangwynne. 2016. Coexisting Liquid Phases Underlie Nucleolar Subcompartments. *Cell*. 165:1686–1697. doi:10.1016/j.cell.2016.04.047.

Galibert, M.D., S. Carreira, and C.R. Goding. 2001. The Usf-1 transcription factor is a novel target for the stress-responsive p38 kinase and mediates UV-induced Tyrosinase expression. *EMBO J*. 20:5022–5031. doi:10.1093/emboj/20.17.5022.

Garden, G.A., M. Hartlage-Rübsamen, E.W. Rubel, and M.A. Bothwell. 1995. Protein masking of a ribosomal RNA epitope is an early event in afferent deprivation-induced neuronal death. *Mol Cell Neurosci*. 6:293–310. doi:10.1006/mcne.1995.1023.

Ginisty, H., H. Sicard, B. Roger, and P. Bouvet. 1999. Structure and functions of nucleolin. *J Cell Sci*. 112 (Pt 6):761–772. doi:10.1242/jcs.112.6.761.

Greco, A. 2009. Involvement of the nucleolus in replication of human viruses. *Rev Med Virol*. 19:201–214. doi:10.1002/rmv.614.

Greco, A., L. Arata, E. Soler, X. Gaume, Y. Couté, S. Hacot, A. Callé, K. Monier, A.L. Epstein, J.-C. Sanchez, P. Bouvet, and J.-J. Diaz. 2012. Nucleolin interacts with US11 protein of herpes simplex virus 1 and is involved in its trafficking. *J Virol*. 86:1449–1457. doi:10.1128/JVI.06194-11.

Harkiolaki, M., M.C. Darrow, M.C. Spink, E. Kosior, K. Dent, and E. Duke. 2018. Cryo-soft X-ray tomography: using soft X-rays to explore the ultrastructure of whole cells. *Emerg Top Life Sci*. 2:81–92. doi:10.1042/ETLS20170086.

Hernandez-Verdun, D. 2011. Assembly and disassembly of the nucleolus during the cell cycle. *Nucleus*. 2:189–194. doi:10.4161/nucl.2.3.16246.

Hindley, C.E., A.D. Davidson, and D.A. Matthews. 2007. Relationship between adenovirus DNA replication proteins and nucleolar proteins B23.1 and B23.2. *J Gen Virol*. 88:3244–3248. doi:10.1099/vir.0.83196-0.

Hiscox, J.A. 2007. RNA viruses: hijacking the dynamic nucleolus. *Nat Rev Microbiol*. 5:119–127. doi:10.1038/nrmicro1597.

Huber, M.D., J.H. Dworet, K. Shire, L. Frappier, and M.A. McAlear. 2000. The budding yeast homolog of the human EBNA1-binding protein 2 (Ebp2p) is an essential nucleolar protein required for pre-rRNA processing. *J Biol Chem*. 275:28764–28773. doi:10.1074/jbc.M000594200.

Iarovaia, O.V., E.S. Ioudinkova, A.K. Velichko, and S.V. Razin. 2021. Manipulation of Cellular Processes via Nucleolus Hijaking in the Course of Viral Infection in Mammals. *Cells*. 10:1597. doi:10.3390/cells10071597.

Iarovaia, O.V., E.P. Minina, E.V. Sheval, D. Onichtchouk, S. Dokudovskaya, S.V. Razin, and Y.S. Vassetzky. 2019. Nucleolus: A Central Hub for Nuclear Functions. *Trends Cell Biol*. 29:647–659. doi:10.1016/j.tcb.2019.04.003.

Ihalainen, T.O., E.A. Niskanen, J. Jylhävä, O. Paloheimo, N. Dross, H. Smolander, J. Langowski, J. Timonen, and M. Vihinen-Ranta. 2009. Parvovirus induced alterations in nuclear architecture and dynamics. *PLoS One*. 4:e5948. doi:10.1371/journal.pone.0005948.

Jaberi-Lashkari, N., B. Lee, F. Aryan, and E. Calo. 2023. An evolutionarily nascent architecture underlying the formation and emergence of biomolecular condensates. *Cell Rep*. 42:112955. doi:10.1016/j.celrep.2023.112955.

Jamison, J.M., J. Gilloteaux, L. Perlaky, M. Thiry, K. Smetana, D. Neal, K. McGuire, and J.L. Summers. 2010. Nucleolar changes and fibrillarin redistribution following apatone treatment of human bladder carcinoma cells. *J Histochem Cytochem*. 58:635–651. doi:10.1369/jhc.2010.956284.

Jia, W., Z. Yao, J. Zhao, Q. Guan, and L. Gao. 2017. New perspectives of physiological and pathological functions of nucleolin (NCL). *Life Sci*. 186:1–10. doi:10.1016/j.lfs.2017.07.025.

Johnson, J.S., and R.J. Samulski. 2009. Enhancement of adeno-associated virus infection by mobilizing capsids into and out of the nucleolus. *J Virol*. 83:2632–2644. doi:10.1128/JVI.02309-08.

Kapur, J.N., P.K. Sahoo, and A.K.C. Wong. 1985. A new method for gray-level picture thresholding using the entropy of the histogram. *Computer Vision, Graphics, and Image Processing*. 29:273–285. doi:10.1016/0734-189X(85)90125-2.

Kellner, M., M. Rohrmoser, I. Forné, K. Voss, K. Burger, B. Mühl, A. Gruber-Eber, E. Kremmer, A. Imhof, and D. Eick. 2015. DEAD-box helicase DDX27 regulates 3’ end formation of ribosomal 47S RNA and stably associates with the PeBoW-complex. *Exp Cell Res*. 334:146–159. doi:10.1016/j.yexcr.2015.03.017.

Kill, I.R. 1996. Localisation of the Ki-67 antigen within the nucleolus. Evidence for a fibrillarin-deficient region of the dense fibrillar component. *J Cell Sci*. 109 (Pt 6):1253–1263. doi:10.1242/jcs.109.6.1253.

Kim, K.-D., H. Tanizawa, A. De Leo, O. Vladimirova, A. Kossenkov, F. Lu, L.C. Showe, K.-I. Noma, and P.M. Lieberman. 2020. Epigenetic specifications of host chromosome docking sites for latent Epstein-Barr virus. *Nat Commun*. 11:877. doi:10.1038/s41467-019-14152-8.

Lafontaine, D.L., and D. Tollervey. 2000. Synthesis and assembly of the box C+D small nucleolar RNPs. *Mol Cell Biol*. 20:2650–2659. doi:10.1128/MCB.20.8.2650-2659.2000.

Lafontaine, D.L.J. 2019. Birth of Nucleolar Compartments: Phase Separation-Driven Ribosomal RNA Sorting and Processing. *Mol Cell*. 76:694–696. doi:10.1016/j.molcel.2019.11.015.

Lafontaine, D.L.J. 2023a. In phase with the nucleolus. *Cell Res*. 33:579–580. doi:10.1038/s41422-023-00801-7.

Lafontaine, D.L.J. 2023b. When two became three: Shaping the nucleolus with Treacle. *Cell Rep*. 42:113060. doi:10.1016/j.celrep.2023.113060.

Lafontaine, D.L.J., J.A. Riback, R. Bascetin, and C.P. Brangwynne. 2021. The nucleolus as a multiphase liquid condensate. *Nat Rev Mol Cell Biol*. 22:165–182. doi:10.1038/s41580-020-0272-6.

Lawrence, F.J., B. McStay, and D.A. Matthews. 2006. Nucleolar protein upstream binding factor is sequestered into adenovirus DNA replication centres during infection without affecting RNA polymerase I location or ablating rRNA synthesis. *Journal of Cell Science*. 119:2621–2631. doi:10.1242/jcs.02982.

Leclerc, S., A. Gupta, V. Ruokolainen, J.-H. Chen, K. Kunnas, A.A. Ekman, H. Niskanen, I. Belevich, H. Vihinen, P. Turkki, A.J. Perez-Berna, S. Kapishnikov, E. Mäntylä, M. Harkiolaki, E. Dufour, V. Hytönen, E. Pereiro, T. McEnroe, K. Fahy, M.U. Kaikkonen, E. Jokitalo, C.A. Larabell, V. Weinhardt, S. Mattola, V. Aho, and M. Vihinen-Ranta. 2024. Progression of herpesvirus infection remodels mitochondrial organization and metabolism. *PLOS Pathogens*. 20:e1011829. doi:10.1371/journal.ppat.1011829.

Lee, T.W.R., G.E. Blair, and D.A. Matthews. 2003. Adenovirus core protein VII contains distinct sequences that mediate targeting to the nucleus and nucleolus, and colocalization with human chromosomes. *J Gen Virol*. 84:3423–3428. doi:10.1099/vir.0.19546-0.

Li, C.H., and C.K. Lee. 1993. Minimum cross entropy thresholding. *Pattern Recognition*. 26:617–625. doi:10.1016/0031-3203(93)90115-D.

Lindström, M.S. 2011. NPM1/B23: A Multifunctional Chaperone in Ribosome Biogenesis and Chromatin Remodeling. *Biochem Res Int*. 2011:195209. doi:10.1155/2011/195209.

Liu, X., K. Salokas, F. Tamene, Y. Jiu, R.G. Weldatsadik, T. Öhman, and M. Varjosalo. 2018. An AP-MS- and BioID-compatible MAC-tag enables comprehensive mapping of protein interactions and subcellular localizations. *Nat Commun*. 9:1188. doi:10.1038/s41467-018-03523-2.

Loconte, V., J. Singla, A. Li, J.-H. Chen, A. Ekman, G. McDermott, A. Sali, M. Le Gros, K.L. White, and C.A. Larabell. 2022. Soft X-ray tomography to map and quantify organelle interactions at the mesoscale. *Structure*. 30:510-521.e3. doi:10.1016/j.str.2022.01.006.

Lymberopoulos, M.H., A. Bourget, N. Ben Abdeljelil, and A. Pearson. 2011. Involvement of the UL24 protein in herpes simplex virus 1-induced dispersal of B23 and in nuclear egress. *Virology*. 412:341–348. doi:10.1016/j.virol.2011.01.016.

Lymberopoulos, M.H., and A. Pearson. 2007. Involvement of UL24 in herpes-simplex-virus-1-induced dispersal of nucleolin. *Virology*. 363:397–409. doi:10.1016/j.virol.2007.01.028.

Lymberopoulos, M.H., and A. Pearson. 2010. Relocalization of upstream binding factor to viral replication compartments is UL24 independent and follows the onset of herpes simplex virus 1 DNA synthesis. *J Virol*. 84:4810–4815. doi:10.1128/JVI.02437-09.

Malik-Soni, N., and L. Frappier. 2014. Nucleophosmin contributes to the transcriptional activation function of the Epstein-Barr virus EBNA1 protein. *J Virol*. 88:2323–2326. doi:10.1128/JVI.02521-13.

Matthews, D., E. Emmott, and J. Hiscox. 2011. Viruses and the Nucleolus. 321–345. doi:10.1007/978-1-4614-0514-6_14.

Mattola, S., E. Mäntylä, V. Aho, S. Salminen, S. Leclerc, M. Oittinen, K. Salokas, J. Järvensivu, S. Hakanen, T.O. Ihalainen, K. Viiri, and M. Vihinen-Ranta. 2022a. G2/M checkpoint regulation and apoptosis facilitate the nuclear egress of parvoviral capsids. *Front Cell Dev Biol*. 10:1070599. doi:10.3389/fcell.2022.1070599.

Mattola, S., K. Salokas, V. Aho, E. Mäntylä, S. Salminen, S. Hakanen, E.A. Niskanen, J. Svirskaite, T.O. Ihalainen, K.J. Airenne, M. Kaikkonen-Määttä, C.R. Parrish, M. Varjosalo, and M. Vihinen-Ranta. 2022b. Parvovirus nonstructural protein 2 interacts with chromatin-regulating cellular proteins. *PLoS Pathog*. 18:e1010353. doi:10.1371/journal.ppat.1010353.

Mellacheruvu, D., Z. Wright, A.L. Couzens, J.-P. Lambert, N.A. St-Denis, T. Li, Y.V. Miteva, S. Hauri, M.E. Sardiu, T.Y. Low, V.A. Halim, R.D. Bagshaw, N.C. Hubner, A. Al-Hakim, A. Bouchard, D. Faubert, D. Fermin, W.H. Dunham, M. Goudreault, Z.-Y. Lin, B.G. Badillo, T. Pawson, D. Durocher, B. Coulombe, R. Aebersold, G. Superti-Furga, J. Colinge, A.J.R. Heck, H. Choi, M. Gstaiger, S. Mohammed, I.M. Cristea, K.L. Bennett, M.P. Washburn, B. Raught, R.M. Ewing, A.-C. Gingras, and A.I. Nesvizhskii. 2013. The CRAPome: a contaminant repository for affinity purification-mass spectrometry data. *Nat Methods*. 10:730–736. doi:10.1038/nmeth.2557.

Mitrea, D.M., J.A. Cika, C.S. Guy, D. Ban, P.R. Banerjee, C.B. Stanley, A. Nourse, A.A. Deniz, and R.W. Kriwacki. 2016. Nucleophosmin integrates within the nucleolus via multi-modal interactions with proteins displaying R-rich linear motifs and rRNA. *Elife*. 5:e13571. doi:10.7554/eLife.13571.

Mitrea, D.M., J.A. Cika, C.B. Stanley, A. Nourse, P.L. Onuchic, P.R. Banerjee, A.H. Phillips, C.-G. Park, A.A. Deniz, and R.W. Kriwacki. 2018. Self-interaction of NPM1 modulates multiple mechanisms of liquid–liquid phase separation. *Nat Commun*. 9:842. doi:10.1038/s41467-018-03255-3.

Mullineux, S.-T., and D.L.J. Lafontaine. 2012. Mapping the cleavage sites on mammalian pre-rRNAs: where do we stand? *Biochimie*. 94:1521–1532. doi:10.1016/j.biochi.2012.02.001.

Naeger, L.K., J. Cater, and D.J. Pintel. 1990. The small nonstructural protein (NS2) of the parvovirus minute virus of mice is required for efficient DNA replication and infectious virus production in a cell-type-specific manner. *J Virol*. 64:6166–6175. doi:10.1128/JVI.64.12.6166-6175.1990.

Niskanen, E.A., T.O. Ihalainen, O. Kalliolinna, M.M. Häkkinen, and M. Vihinen-Ranta. 2010. Effect of ATP binding and hydrolysis on dynamics of canine parvovirus NS1. *J Virol*. 84:5391–5403. doi:10.1128/JVI.02221-09.

Niskanen, E.A., O. Kalliolinna, T.O. Ihalainen, M. Häkkinen, and M. Vihinen-Ranta. 2013. Mutations in DNA binding and transactivation domains affect the dynamics of parvovirus NS1 protein. *J Virol*. 87:11762–11774. doi:10.1128/JVI.01678-13.

O'Connor, S., D. Rogers, M. Kobylynska, J. Geraets, K. Thaysen, J.M. Egebjerg, M.C. Brink, L. Herbsleb, M. Salakova, L. Fuchs, F. Alves, C. Feldmann, A. Ekman, P. Sheridan, W. Fyans, T. McEnroe, F. O'Reily, K. Fahy, R.A. Fleck, D. Wüstner, J.C. Simpson, A. Walter, and S. Kapishnikov. 2024. Demonstrating Soft X-Ray Tomography in the lab for correlative cryogenic biological imaging using X-rays and light microscopy. 2024.12.23.629889. doi:10.1101/2024.12.23.629889.

Omer, A.D., S. Ziesche, H. Ebhardt, and P.P. Dennis. 2002. In vitro reconstitution and activity of a C/D box methylation guide ribonucleoprotein complex. *Proc Natl Acad Sci U S A*. 99:5289–5294. doi:10.1073/pnas.082101999.

Otsu, N. 1979. A Threshold Selection Method from Gray-Level Histograms. *IEEE Transactions on Systems, Man, and Cybernetics*. 9:62–66. doi:10.1109/TSMC.1979.4310076.

Padeken, J., and P. Heun. 2014. Nucleolus and nuclear periphery: velcro for heterochromatin. *Curr Opin Cell Biol*. 28:54–60. doi:10.1016/j.ceb.2014.03.001.

Pan, W.-A., H.-Y. Tsai, S.-C. Wang, M. Hsiao, P.-Y. Wu, and M.-D. Tsai. 2015. The RNA recognition motif of NIFK is required for rRNA maturation during cell cycle progression. *RNA Biol*. 12:255–267. doi:10.1080/15476286.2015.1017221.

Parrish, C.R. 1991. Mapping specific functions in the capsid structure of canine parvovirus and feline panleukopenia virus using infectious plasmid clones. *Virology*. 183:195–205. doi:10.1016/0042-6822(91)90132-u.

Pearson, A., A. Bourget, N. Ben Abdeljelil, and M.H. Lymberopoulos. 2011. Role of the viral protein UL24 in nucleolar modifications induced by herpes simplex virus 1. *BMC Proceedings*. 5:P102. doi:10.1186/1753-6561-5-S1-P102.

Pederson, T. 2011. The nucleolus. *Cold Spring Harb Perspect Biol*. 3:a000638. doi:10.1101/cshperspect.a000638.

Peng, T., Y. Hou, H. Meng, Y. Cao, X. Wang, L. Jia, Q. Chen, Y. Zheng, Y. Sun, H. Chen, T. Li, and C. Li. 2023. Mapping nucleolus-associated chromatin interactions using nucleolus Hi-C reveals pattern of heterochromatin interactions. *Nat Commun*. 14:350. doi:10.1038/s41467-023-36021-1.

Phair, R.D., and T. Misteli. 2000. High mobility of proteins in the mammalian cell nucleus. *Nature*. 404:604–609. doi:10.1038/35007077.

Qi, Y., and B. Zhang. 2021. Chromatin network retards nucleoli coalescence. *Nat Commun*. 12:6824. doi:10.1038/s41467-021-27123-9.

Qiu, J., and K.E. Brown. 1999. A 110-kDa nuclear shuttle protein, nucleolin, specifically binds to adeno-associated virus type 2 (AAV-2) capsid. *Virology*. 257:373–382. doi:10.1006/viro.1999.9664.

Raska, I., P.J. Shaw, and D. Cmarko. 2006. Structure and function of the nucleolus in the spotlight. *Curr Opin Cell Biol*. 18:325–334. doi:10.1016/j.ceb.2006.04.008.

Rawlinson, S.M., T. Zhao, A.M. Rozario, C.L. Rootes, P.J. McMillan, A.W. Purcell, A. Woon, G.A. Marsh, K.G. Lieu, L.-F. Wang, H.J. Netter, T.D.M. Bell, C.R. Stewart, and G.W. Moseley. 2018. Viral regulation of host cell biology by hijacking of the nucleolar DNA-damage response. *Nat Commun*. 9:3057. doi:10.1038/s41467-018-05354-7.

Remnant, L., N.Y. Kochanova, C. Reid, F. Cisneros-Soberanis, and W.C. Earnshaw. 2021. The intrinsically disorderly story of Ki-67. *Open Biol*. 11:210120. doi:10.1098/rsob.210120.

Roussel, P., C. André, C. Masson, G. Géraud, and D. Hernandez-Verdun. 1993. Localization of the RNA polymerase I transcription factor hUBF during the cell cycle. *J Cell Sci*. 104 (Pt 2):327–337. doi:10.1242/jcs.104.2.327.

Sagou, K., M. Uema, and Y. Kawaguchi. 2010. Nucleolin is required for efficient nuclear egress of herpes simplex virus type 1 nucleocapsids. *J Virol*. 84:2110–2121. doi:10.1128/JVI.02007-09.

Salvetti, A., and A. Greco. 2014. Viruses and the nucleolus: the fatal attraction. *Biochim Biophys Acta*. 1842:840–847. doi:10.1016/j.bbadis.2013.12.010.

Sanij, E., and R.D. Hannan. 2009. The role of UBF in regulating the structure and dynamics of transcriptionally active rDNA chromatin. *Epigenetics*. 4:374–382. doi:10.4161/epi.4.6.9449.

Sanij, E., G. Poortinga, K. Sharkey, S. Hung, T.P. Holloway, J. Quin, E. Robb, L.H. Wong, W.G. Thomas, V. Stefanovsky, T. Moss, L. Rothblum, K.M. Hannan, G.A. McArthur, R.B. Pearson, and R.D. Hannan. 2008. UBF levels determine the number of active ribosomal RNA genes in mammals. *The Journal of Cell Biology*. 183:1259–1274. doi:10.1083/jcb.200805146.

van Schaik, T., S.G. Manzo, A.E. Vouzas, N.Q. Liu, H. Teunissen, E. de Wit, D.M. Gilbert, and B. van Steensel. 2022. Dynamic chromosomal interactions and control of heterochromatin positioning by Ki-67. *EMBO Rep*. 23:e55782. doi:10.15252/embr.202255782.

Scherl, A., Y. Couté, C. Déon, A. Callé, K. Kindbeiter, J.-C. Sanchez, A. Greco, D. Hochstrasser, and J.-J. Diaz. 2002. Functional proteomic analysis of human nucleolus. *Mol Biol Cell*. 13:4100–4109. doi:10.1091/mbc.e02-05-0271.

Schindelin, J., I. Arganda-Carreras, E. Frise, V. Kaynig, M. Longair, T. Pietzsch, S. Preibisch, C. Rueden, S. Saalfeld, B. Schmid, J.-Y. Tinevez, D.J. White, V. Hartenstein, K. Eliceiri, P. Tomancak, and A. Cardona. 2012. Fiji: an open-source platform for biological-image analysis. *Nat Methods*. 9:676–682. doi:10.1038/nmeth.2019.

Shan, L., G. Xu, R.-W. Yao, P.-F. Luan, Y. Huang, P.-H. Zhang, Y.-H. Pan, L. Zhang, X. Gao, Y. Li, S.-M. Cao, S.-X. Gao, Z.-H. Yang, S. Li, L.-Z. Yang, Y. Wang, C.C.L. Wong, L. Yu, J. Li, L. Yang, and L.-L. Chen. 2023. Nucleolar URB1 ensures 3' ETS rRNA removal to prevent exosome surveillance. *Nature*. 615:526–534. doi:10.1038/s41586-023-05767-5.

Sheard, T.M.D., T.B. Shakespeare, R.S. Seehra, M.E. Spencer, K.M. Suen, and I. Jayasinghe. 2023. Differential labelling of human sub-cellular compartments with fluorescent dye esters and expansion microscopy. *Nanoscale*. 15:18489–18499. doi:10.1039/d3nr01129a.

Sobecki, M., K. Mrouj, A. Camasses, N. Parisis, E. Nicolas, D. Llères, F. Gerbe, S. Prieto, L. Krasinska, A. David, M. Eguren, M.-C. Birling, S. Urbach, S. Hem, J. Déjardin, M. Malumbres, P. Jay, V. Dulic, D.L. Lafontaine, R. Feil, and D. Fisher. 2016. The cell proliferation antigen Ki-67 organises heterochromatin. *Elife*. 5:e13722. doi:10.7554/eLife.13722.

Söderberg, O., M. Gullberg, M. Jarvius, K. Ridderstråle, K.-J. Leuchowius, J. Jarvius, K. Wester, P. Hydbring, F. Bahram, L.-G. Larsson, and U. Landegren. 2006. Direct observation of individual endogenous protein complexes in situ by proximity ligation. *Nat Methods*. 3:995–1000. doi:10.1038/nmeth947.

Srivastava, M., and H.B. Pollard. 1999. Molecular dissection of nucleolin's role in growth and cell proliferation: new insights. *FASEB J*. 13:1911–1922.

Stenström, L., D. Mahdessian, C. Gnann, A.J. Cesnik, W. Ouyang, M.D. Leonetti, M. Uhlén, S. Cuylen-Haering, P.J. Thul, and E. Lundberg. 2020. Mapping the nucleolar proteome reveals a spatiotemporal organization related to intrinsic protein disorder. *Mol Syst Biol*. 16:e9469. doi:10.15252/msb.20209469.

Stow, N.D., V.C. Evans, and D.A. Matthews. 2009. Upstream-binding factor is sequestered into herpes simplex virus type 1 replication compartments. *J Gen Virol*. 90:69–73. doi:10.1099/vir.0.006353-0.

Strom, A.R., and C.P. Brangwynne. 2019. The liquid nucleome - phase transitions in the nucleus at a glance. *J Cell Sci*. 132:jcs235093. doi:10.1242/jcs.235093.

Sun, X., and P.D. Kaufman. 2018. Ki-67: more than a proliferation marker. *Chromosoma*. 127:175–186. doi:10.1007/s00412-018-0659-8.

Takagi, M., M. Sueishi, T. Saiwaki, A. Kametaka, and Y. Yoneda. 2001. A novel nucleolar protein, NIFK, interacts with the forkhead associated domain of Ki-67 antigen in mitosis. *J Biol Chem*. 276:25386–25391. doi:10.1074/jbc.M102227200.

Tchelidze, P., A. Benassarou, H. Kaplan, M.-F. O'Donohue, L. Lucas, C. Terryn, L. Rusishvili, G. Mosidze, N. Lalun, and D. Ploton. 2017. Nucleolar sub-compartments in motion during rRNA synthesis inhibition: Contraction of nucleolar condensed chromatin and gathering of fibrillar centers are concomitant. *PLoS One*. 12:e0187977. doi:10.1371/journal.pone.0187977.

Teo, G., G. Liu, J. Zhang, A.I. Nesvizhskii, A.-C. Gingras, and H. Choi. 2014. SAINTexpress: improvements and additional features in Significance Analysis of INTeractome software. *J Proteomics*. 100:37–43. doi:10.1016/j.jprot.2013.10.023.

Thiry, M. 1993. Ultrastructural distribution of DNA and RNA within the nucleolus of human Sertoli cells as seen by molecular immunocytochemistry. *J Cell Sci*. 105 (Pt 1):33–39. doi:10.1242/jcs.105.1.33.

Thiry, M., and D.L.J. Lafontaine. 2005. Birth of a nucleolus: the evolution of nucleolar compartments. *Trends in Cell Biology*. 15:194–199. doi:10.1016/j.tcb.2005.02.007.

Thoms, M., R. Buschauer, M. Ameismeier, L. Koepke, T. Denk, M. Hirschenberger, H. Kratzat, M. Hayn, T. Mackens-Kiani, J. Cheng, J.H. Straub, C.M. Stürzel, T. Fröhlich, O. Berninghausen, T. Becker, F. Kirchhoff, K.M.J. Sparrer, and R. Beckmann. 2020. Structural basis for translational shutdown and immune evasion by the Nsp1 protein of SARS-CoV-2. *Science*. 369:1249–1255. doi:10.1126/science.abc8665.

Tollervey, D., H. Lehtonen, R. Jansen, H. Kern, and E.C. Hurt. 1993. Temperature-sensitive mutations demonstrate roles for yeast fibrillarin in pre-rRNA processing, pre-rRNA methylation, and ribosome assembly. *Cell*. 72:443–457. doi:10.1016/0092-8674(93)90120-f.

Tuan, J.C., W. Zhai, and L. Comai. 1999. Recruitment of TATA-binding protein-TAFI complex SL1 to the human ribosomal DNA promoter is mediated by the carboxy-terminal activation domain of upstream binding factor (UBF) and is regulated by UBF phosphorylation. *Mol Cell Biol*. 19:2872–2879. doi:10.1128/MCB.19.4.2872.

Uchihara, Y., K. Tago, H. Tamura, and M. Funakoshi-Tago. 2021. EBP2, a novel NPM-ALK-interacting protein in the nucleolus, contributes to the proliferation of ALCL cells by regulating tumor suppressor p53. *Mol Oncol*. 15:167–194. doi:10.1002/1878-0261.12822.

Verheijen, R., H.J. Kuijpers, R. van Driel, J.L. Beck, J.H. van Dierendonck, G.J. Brakenhoff, and F.C. Ramaekers. 1989. Ki-67 detects a nuclear matrix-associated proliferation-related antigen. II. Localization in mitotic cells and association with chromosomes. *J Cell Sci*. 92 (Pt 4):531–540. doi:10.1242/jcs.92.4.531.

Wang, D., W. Yuan, I. Davis, and C.R. Parrish. 1998. Nonstructural protein-2 and the replication of canine parvovirus. *Virology*. 240:273–281. doi:10.1006/viro.1997.8946.

Weichert, W.S., J.S. Parker, A.T. Wahid, S.F. Chang, E. Meier, and C.R. Parrish. 1998. Assaying for structural variation in the parvovirus capsid and its role in infection. *Virology*. 250:106–117. doi:10.1006/viro.1998.9352.

Wistuba, A., A. Kern, S. Weger, D. Grimm, and J.A. Kleinschmidt. 1997. Subcellular compartmentalization of adeno-associated virus type 2 assembly. *J Virol*. 71:1341–1352. doi:10.1128/JVI.71.2.1341-1352.1997.

Yang, K., M. Wang, Y. Zhao, X. Sun, Y. Yang, X. Li, A. Zhou, H. Chu, H. Zhou, J. Xu, M. Wu, J. Yang, and J. Yi. 2016. A redox mechanism underlying nucleolar stress sensing by nucleophosmin. *Nat Commun*. 7:13599. doi:10.1038/ncomms13599.

Yao, R.-W., G. Xu, Y. Wang, L. Shan, P.-F. Luan, Y. Wang, M. Wu, L.-Z. Yang, Y.-H. Xing, L. Yang, and L.-L. Chen. 2019. Nascent Pre-rRNA Sorting via Phase Separation Drives the Assembly of Dense Fibrillar Components in the Human Nucleolus. *Molecular Cell*. 76:767-783.e11. doi:10.1016/j.molcel.2019.08.014.

Yao, Z., S. Duan, D. Hou, W. Wang, G. Wang, Y. Liu, L. Wen, and M. Wu. 2010. B23 acts as a nucleolar stress sensor and promotes cell survival through its dynamic interaction with hnRNPU and hnRNPA1. *Oncogene*. 29:1821–1834. doi:10.1038/onc.2009.473.

Yeung, D.E., G.W. Brown, P. Tam, R.H. Russnak, G. Wilson, I. Clark-Lewis, and C.R. Astell. 1991. Monoclonal antibodies to the major nonstructural nuclear protein of minute virus of mice. *Virology*. 181:35–45. doi:10.1016/0042-6822(91)90467-p.

Figure legends

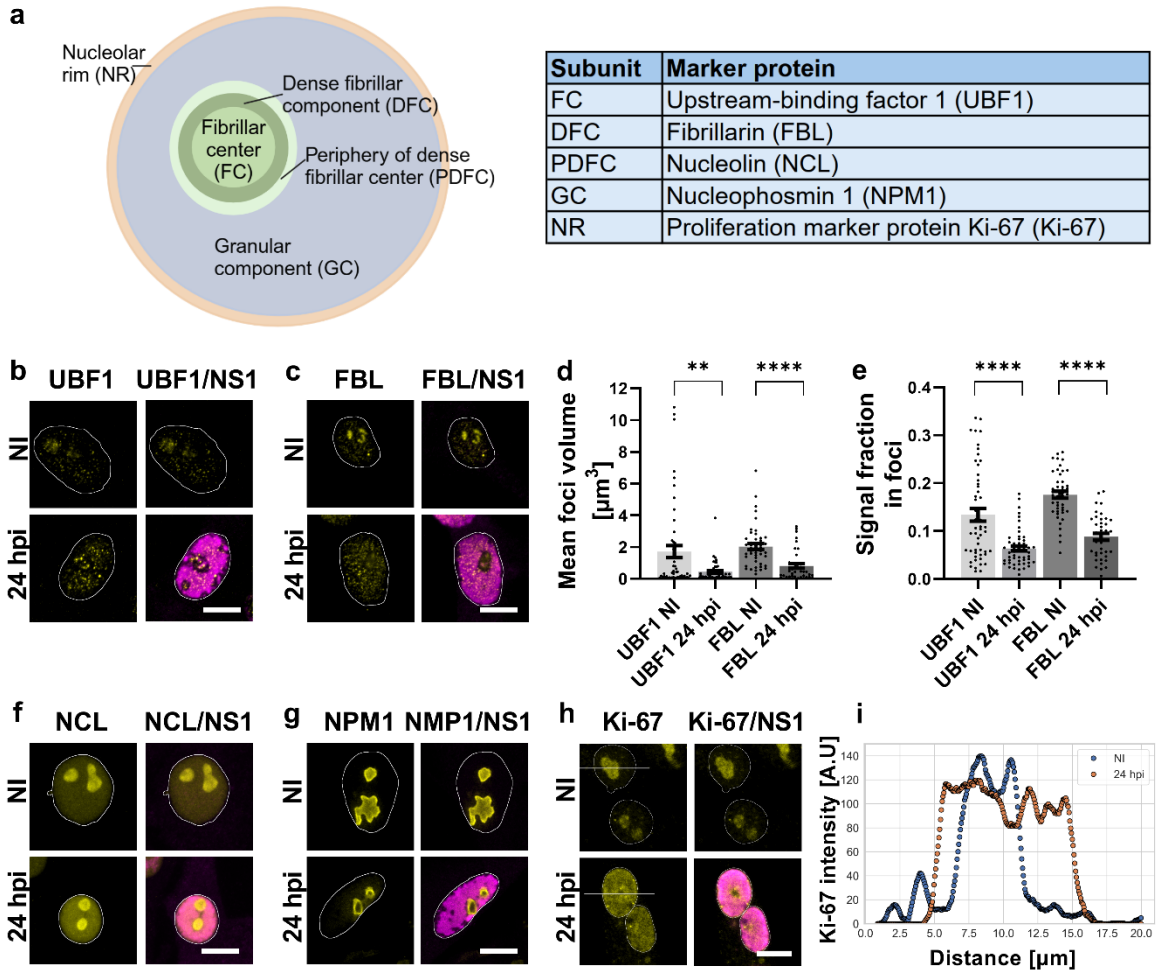

Subunit	Marker protein
FC	Upstream-binding factor 1 (UBF1)
DFC	Fibrillarin (FBL)
PDFC	Nucleolin (NCL)
GC	Nucleophosmin 1 (NPM1)
NR	Proliferation marker protein Ki-67 (Ki-67)

Figure 1. Nucleolar protein distribution changes during CPV infection

(**a**) Schematic of distribution of nucleolar proteins upstream-binding factor 1 (UBF1), fibrillarin (FBL), nucleolin (NCL), nucleophosmin 1 (NPM1), and Ki-67 in nucleolar subcompartments: the fibrillar center (FC), the dense fibrillar component (DFC), the periphery of the dense fibrillar center (PDFC), the granular component (GC), and the nucleolar rim (NR). Representative confocal maximum intensity projections showing the distribution of (**b**) UBF1 and (**c**) FBL in noninfected (NI) and infected NLFK cells at 24 hpi. (**d**) Quantitative analyses of the mean volume of UBF1 and FBL foci, and (**e**) the fraction of nuclear UBF1 and FBL signal detected in the foci in noninfected and infected cells at 24 hpi (n_{NI} = 52, 46 and n_{inf} = 52, 40, respectively). Distribution of (**f**) NCL, (**g**) NPM1, and (**h**) Ki-67 in noninfected and infected cells at 24 hpi. (**i**) Representative Ki-67 intensity line profiles of noninfected (blue) and infected cells (orange) at 24 hpi. The cells were immunolabeled with antibodies against UBF1, FBL, NCL, NPM1, Ki-67 (yellow), and the viral NS1 protein (a marker of viral replication compartment region, magenta) antibodies. DNA was labeled with DAPI, and a white line illustrates the borders of the nuclei. Scale bar, 10 µm. The error bars show the standard error of the mean. Statistical significance was determined using Welch's *t*-test. The significance values shown are denoted as **** ($p<0.0001$) or ** ($p=0.0021$).

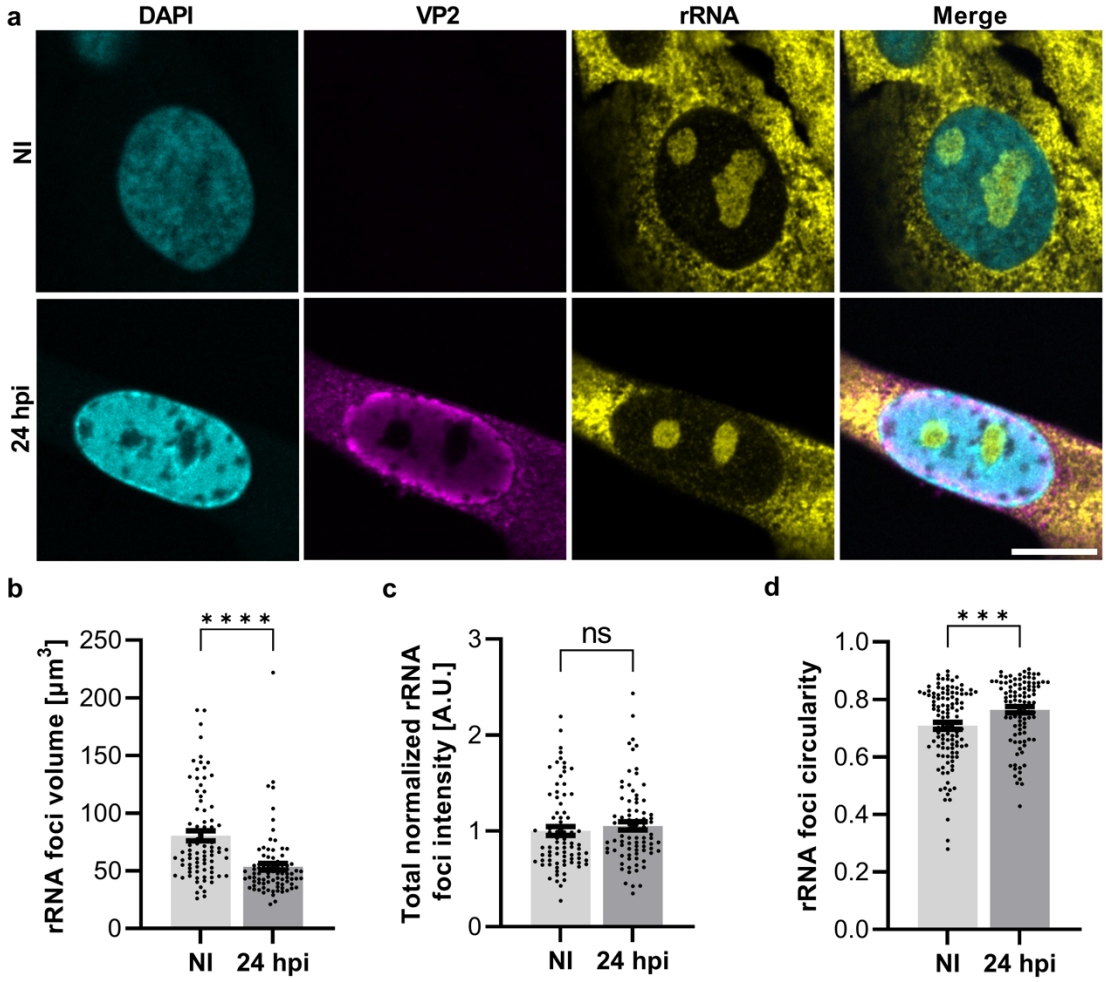

Figure 2. Infection decreases the size and increases the circularity of nucleolar rRNA-positive regions

(**a**) The representative confocal images show the distribution of viral capsids and rRNA in noninfected and infected NLFK cells at 24 hpi. The cells were stained with the viral capsid protein VP2 (magenta) and rRNA (yellow) antibodies. The chromatin was labeled with DAPI

(cyan). Scale bar, 10 µm. (b) The mean volume, and (c) the total normalized intensity of segmented rRNA foci in noninfected and infected cells (n = 82 and 84, respectively). (d) The circularity of the rRNA-labeled segmented nucleoli cross-sections in noninfected and infected cells at 24 hpi (n =115 and 100, respectively). The error bars show the standard error of the mean. Statistical significance was determined using Welch's *t*-test. The significance values shown are denoted as **** ($p<0.0001$), *** ($p=0.0009$), or ns (not significant).

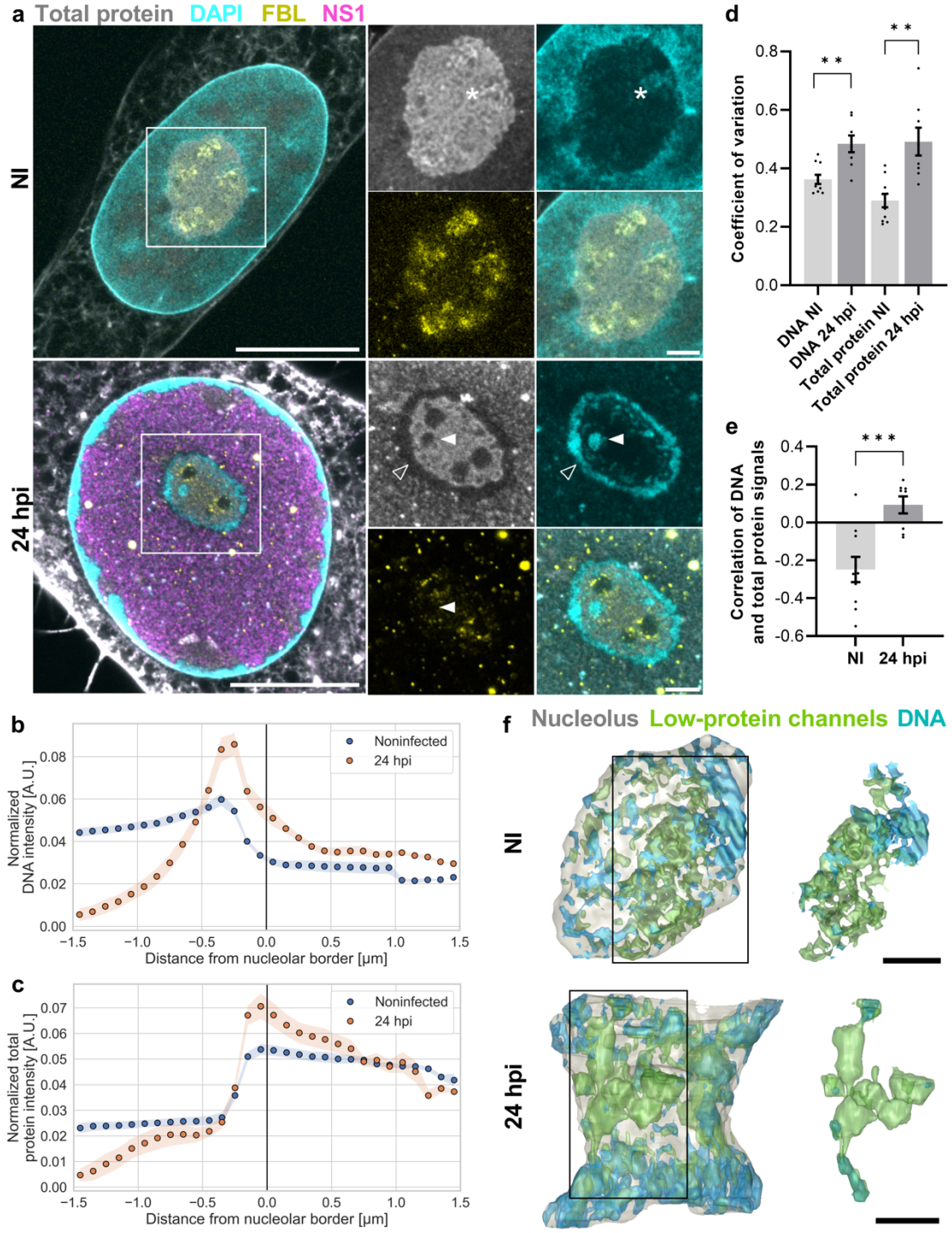

Figure 3. Intranucleolar ultrastructure and chromatin distribution are remodeled in infection

(**a**) Visualization of the nucleolar structure by ten-fold robust expansion microscopy (TREx) in noninfected (NI) and infected NLFK cells at 24 hpi. The representative images show nuclear and nucleolar ultrastructures with the NHS ester total protein stain (gray), DNA staining by DAPI (cyan), and fibrillarin and viral NS1 staining by antibodies (yellow and magenta, respectively). The light areas in total protein-stained cells indicate the presence of highly concentrated protein, and dark areas indicate relatively small amounts of proteins. The final

expansion was estimated to be ~7.5-fold. The localization of nucleolar chromatin in noninfected cells (asterisks), perinucleolar chromatin (empty arrowheads), and nucleolar chromatin (filled arrowheads) in infected cells are shown. The intensities in each image have been independently adjusted for visualization purposes. Scale bars (adjusted to expansion factor), 5 µm and 1 µm. The mean normalized intensity of (**b**) DAPI-labeled DNA and (**c**) total protein as a function of the distance from the nucleolar border in noninfected and infected cells at 24 hpi (n = 10 and 8, respectively). (**d**) The distribution and dispersion of nucleolar DNA and total protein were measured using a coefficient of variation in noninfected and infected cells at 24 hpi. (**e**) DNA and total protein signal correlation in the nucleoli of noninfected and infected cells at 24 hpi (**f**) 3D reconstructions of TREx data show low-protein regions (green) and DAPI DNA stain (blue) in the nucleoli (grey) of noninfected and infected cells. Images on the right depict a single continuous low-protein channel network. Scale bar (adjusted to expansion factor), 1 µm. See also Supplementary Movie 1. The nucleolar segmentation was based on the total protein staining. The error bars show the standard error of the mean. Statistical significance was determined using Welch's *t*-test. The significance values shown are denoted as ***(p=0.0007) or ** (p=0.0034, p= 0.0033).

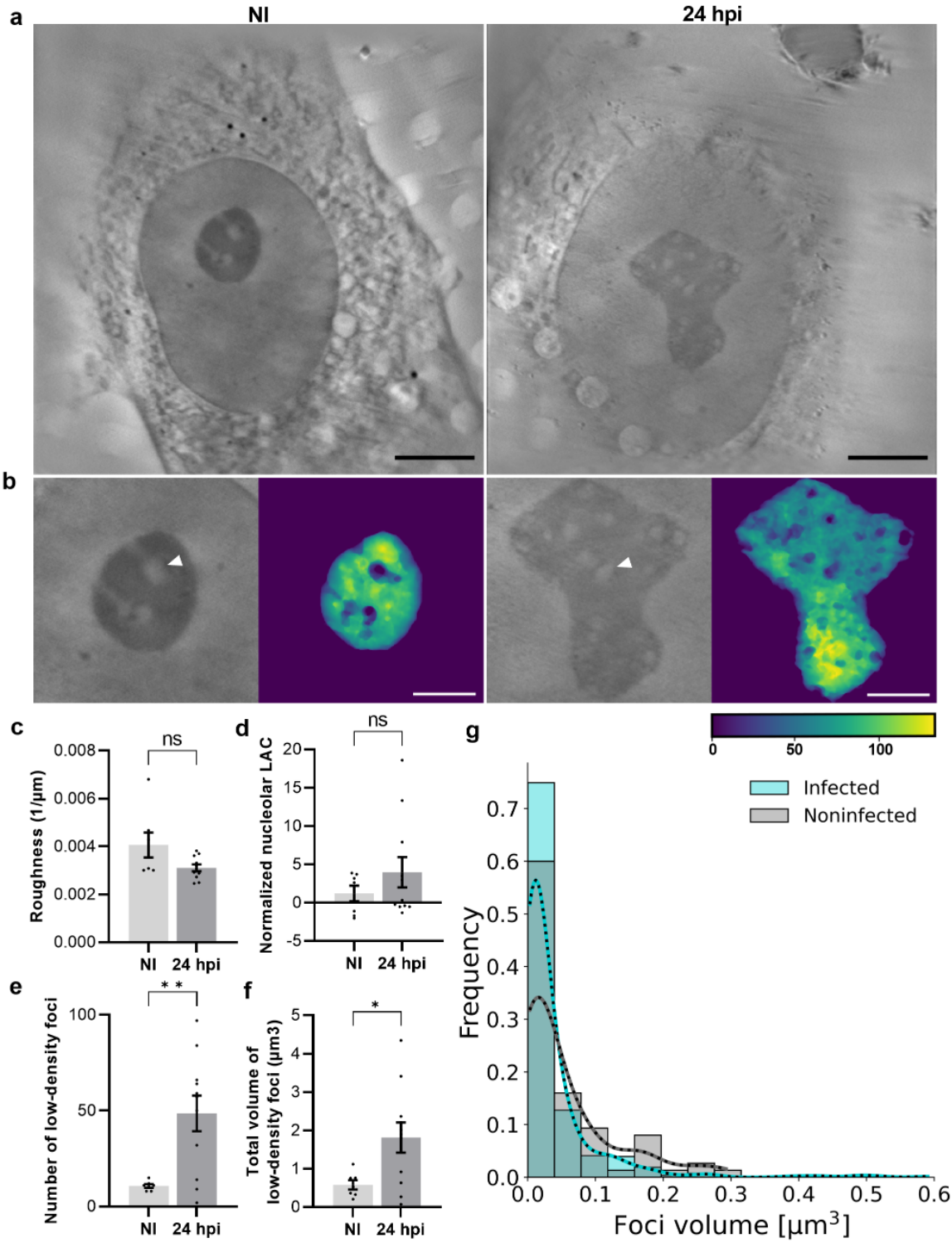

Figure 4. The progression of infection leads to appearance of small nucleolar foci with low density

(**a**) Cryo-soft X-ray tomography (SXT) thin slices (orthoslices) of nucleus and nucleoli in noninfected and infected NLFK cells grown on EM grids at 24 hpi. Scale bars, 5 µm. (**b**) Enlarged insets of SXT images of nucleoli and reconstruction of nucleolar thickness in noninfected and infected cells. The localization of nucleolar low-density foci and regions (filled arrowheads) are shown. The color scale indicates the thickness on the Z-axis (yellow, blue). Scale bars, 2.5 µm. See also Supplementary Movie M2. (**c**) Surface-to-volume ratio analysis

of nucleolar roughness. (**d**) Nucleolar linear absorption coefficient LAC values, (**e**) the number, and (**f**) total volume of intranucleolar low-density foci. (**g**) The normalized number of various-sized nucleolar low-density foci in noninfected and infected cells ($n_{NI} = 6$, $n_{inf} = 7$). The error bars show the standard error of the mean. Statistical significance was determined using Welch's *t*-test. The significance values shown are denoted as ** (p=0.0023), * (p=0.0114), or ns (not significant).

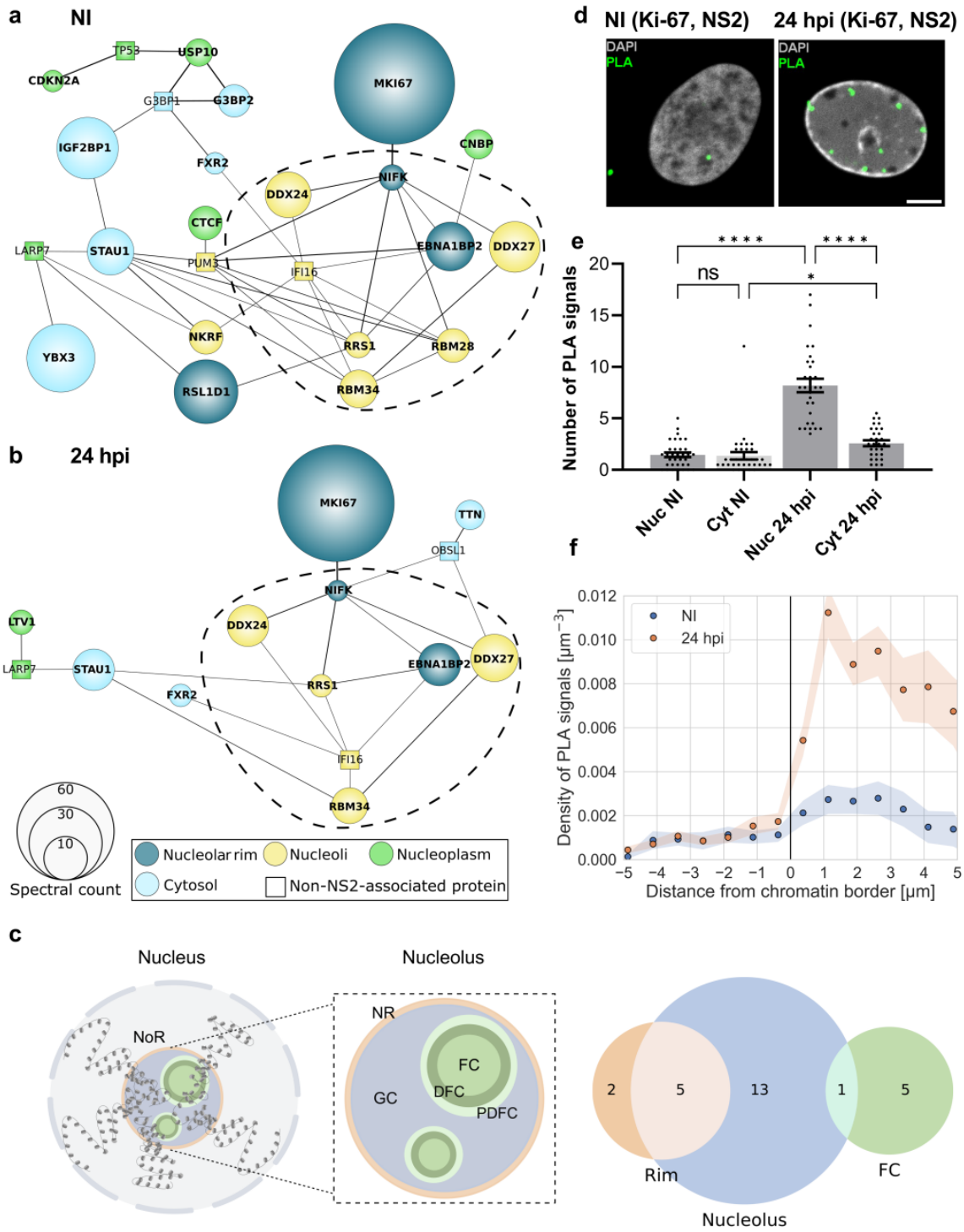

Figure 5. Nucleolar interactions of the viral NS2 protein

Schematic presentation of high-confidence BioID NS2 interactors related to nucleolar processes. Interactors of BirA*-tagged NS2 in (**a**) noninfected (NI) and (**b**) infected Flp-In T-REx 293 cells at 24 hpi are shown. All cells were transfected with BirA*-tagged NS2. Interactor proteins are presented by their gene names. The cellular distribution of NS2-associated nucleolar (round-shaped nodes) and nonnucleolar proteins (square-shaped nodes) in the nucleolar rim (dark blue), nucleoli (yellow), nucleoplasm (green), and cytosol (light blue) is shown. The node size correlates with interaction probability measured by spectral counts, and the black lines between nodes are proportional to the interaction in the STRING database (https://string-db.org/). Interactors are presented by their gene names. (**c**) A schematic image of the organization of the nucleolus organizer region (NoR), nucleolus, and its subcompartments: the fibrillar centre (FC), the dense fibrillar component (DFC), the periphery of dense fibrillar center (PDFC), the granular component (GC), and nucleolar rim (NR). The Venn diagram shows the nucleolar localization of NS2-associated proteins identified by BioID in infected cells at 24 hpi. The numbers of proteins localized into the whole nucleolus (blue), FC and DFC (green), nucleolar rim (orange), or dual localization (light brown, light green) are shown. (**d**) Representative confocal microscopy images showing the nuclear distribution of proximity ligation assay (PLA) foci indicating the interaction between NS2 and Ki-67 in noninfected and infected cells at 24 hpi. Scale bar, 5 µm. (**e**) The number of PLA signals in the nucleus and cytoplasm. (**f**) The density of the PLA foci as a function of increasing distance from the NE in noninfected and infected cells (n = 62 and n = 58, respectively). The error bars and the shaded areas around the data points show the standard error of the mean. Statistical significance was determined using the Games-Howell test. The significance values shown are denoted as **** ($p<0.001$) or * ($p=0.0439$), or ns (not significant).

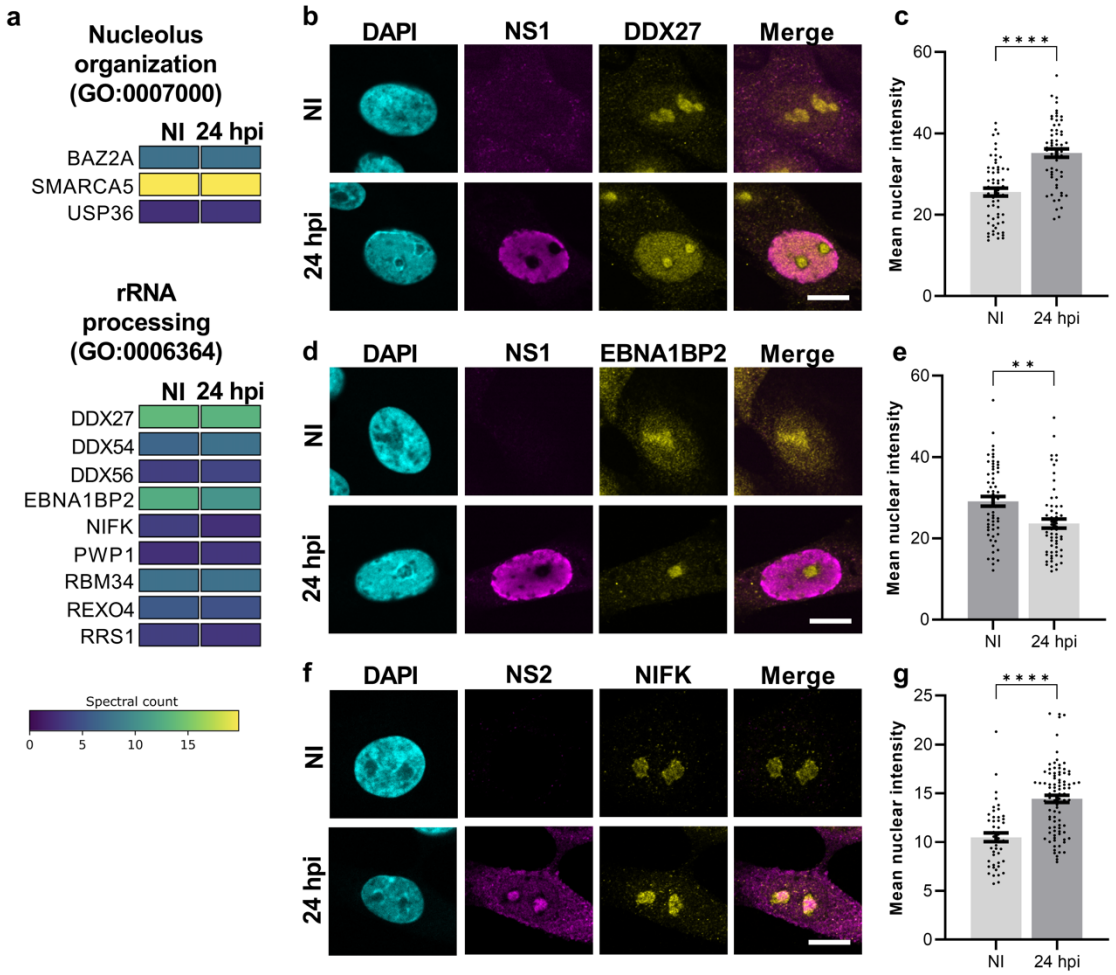

Figure 6. Distribution and intensity of NS2 interactor proteins are altered upon infection

(a) Identification of the viral NS2 protein nucleolar protein interactome using BioID. GO term classification for 12 high-confidence BioID NS2 interactors related to nucleolus organization and rRNA processing. Interactors of BirA*-tagged NS2 in noninfected and infected Flp-In T-REx 293 cells at 24 hpi are shown. The color bar indicates increased interaction (yellow-green) and decreased interaction (green-blue). Interactors are presented by their gene names. (b) Representative confocal images of nuclear localization of DEAD-box helicase DDX27 and (c) its mean nuclear intensity in noninfected and infected NLFK cells at 24 hpi (n = 62). (d) Nuclear distribution and (e) the mean nuclear intensity EBNA1BP2 in noninfected and infected cells (n = 59). (f) Nuclear localization and (g) the mean nuclear intensity of NIFK in noninfected and infected cells (n = 47 and 92, respectively). The cells were immunolabeled with DDX27 (yellow), EBNA1BP2 (yellow), NIFK (yellow), and viral NS1 and NS2 protein (magenta) antibodies. DNA was labeled with DAPI (cyan). Scale bars, 10 µm. The error bars show the standard error of the mean. Statistical significance was determined using Welch's t-test. The significance values shown are denoted as **** ($p<0.0001$) and ** ($p=0.0013<0.01$).

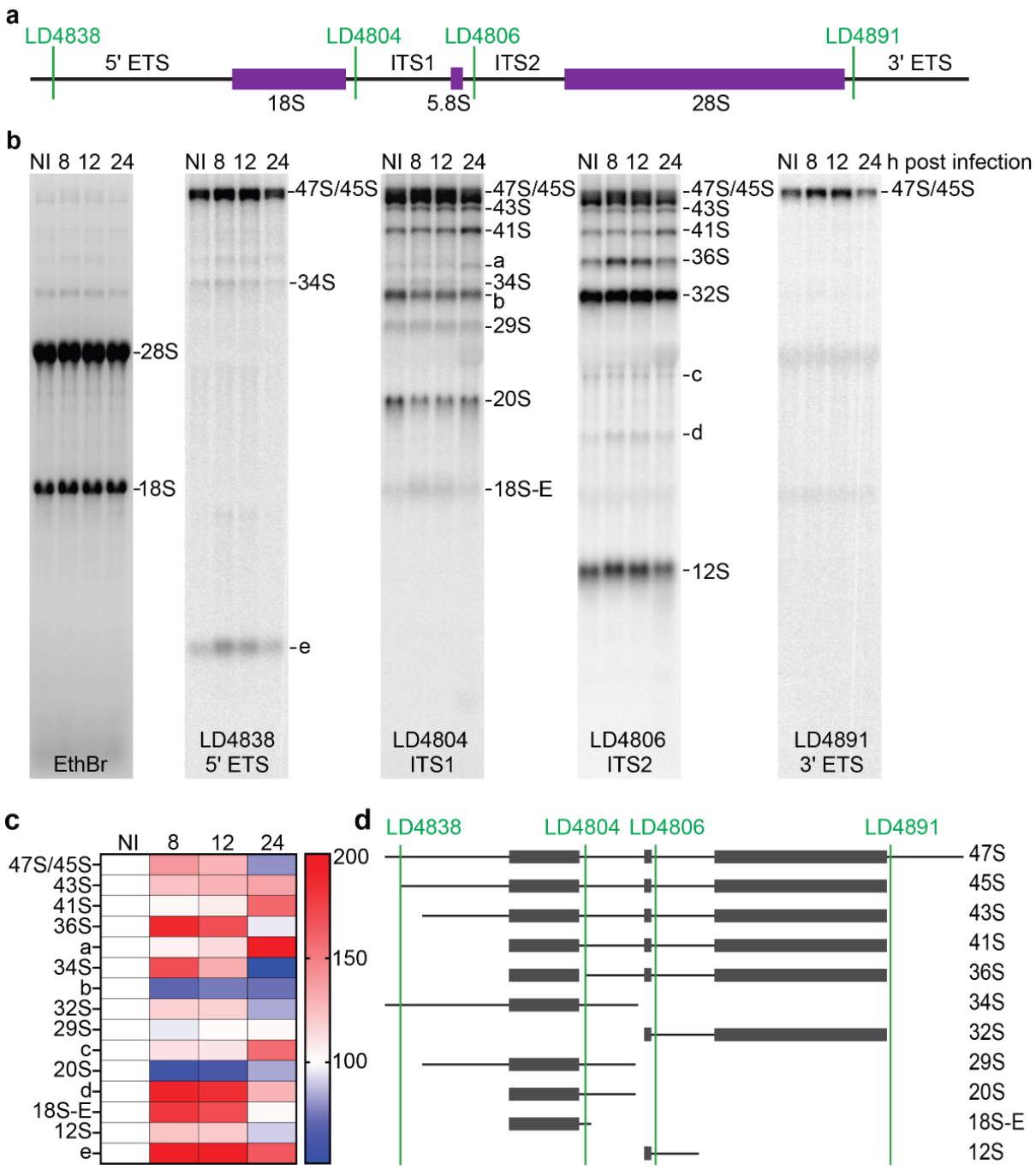

Fig 7. Infection alters ribosome biogenesis

(a) Schematic depiction of the feline 47S pre-rRNA and location of the probes used to detect processing intermediates. The 5' and 3' external transcribed spacers (ETS) and internal transcribed spacers (ITS) 1 and 2 are indicated. (b) Total RNA from NLFK cells was extracted at 8, 12, and 24 hpi. A noninfected (NI) sample was used as a control. The RNA was resolved on a denaturing high-resolution agarose gel, stained with ethidium bromide (EthBr) to reveal large mature rRNAs, or processed for northern blotting to detect precursor rRNAs. Probes for each spacer (LD4838, LD4804, LD4806, and LD4891) were designed (see Materials and Methods), revealing primary processing intermediates. Unmapped species are labeled 'a' to 'e' in order of decreasing size. (c) Phosphorimager quantification of pre-rRNA species detected. The experiment was repeated four times (n= 4, see Fig S7), and the mean values are depicted in the heatmap. A similar processing phenotype can be observed in cells 8 and 12 hpi. At 24 hpi, a different processing phenotype can be observed. (d) Putative pre-rRNA processing

pathway in feline cells, based on a closely related vertebrate mouse (Inspired by Anikin and Pestov, 2022).

Supplementary Figures, tables, and movie legends

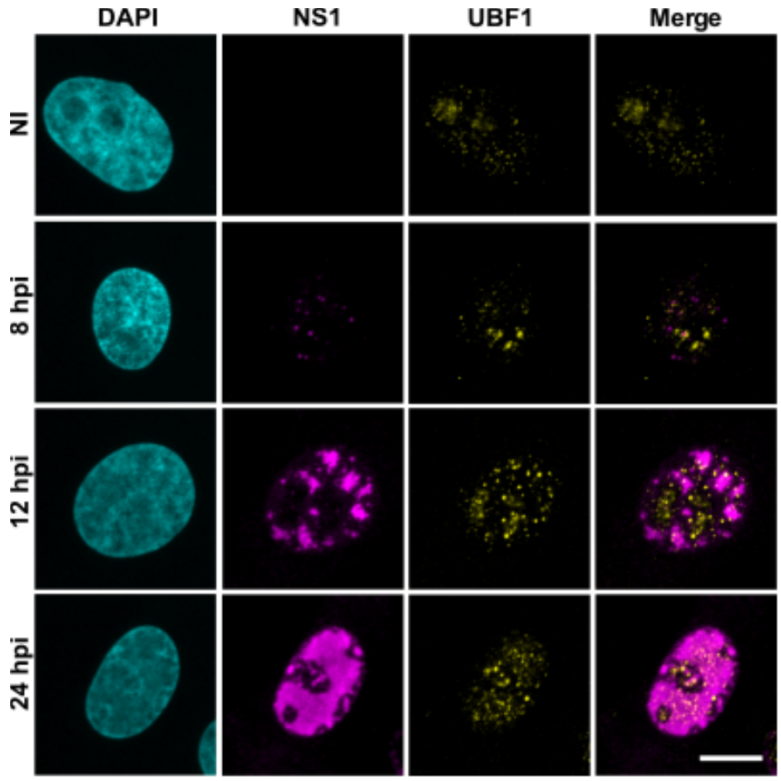

Figure S1. The inner core of the nucleolus is disassembled upon CPV infection, leading to redistribution of UBF1 in the nucleoplasm
Representative confocal maximum intensity projections showing FC marker protein, upstream-binding factor 1 (UBF1), localization in noninfected (NI) and infected NLFK cells at 8, 12, and 24 hpi. The cells were immunolabeled with UBF1 (yellow) and the viral NS1 protein (magenta) antibodies. DNA was labeled with DAPI (cyan). In the NS1 channel, individual VRC (white arrow, 8 hpi) progressively merge into larger structures (12 hpi) to fill in the entire nucleoplasm (24 hpi) as the infection proceeds. Scale bar, 10 µm.

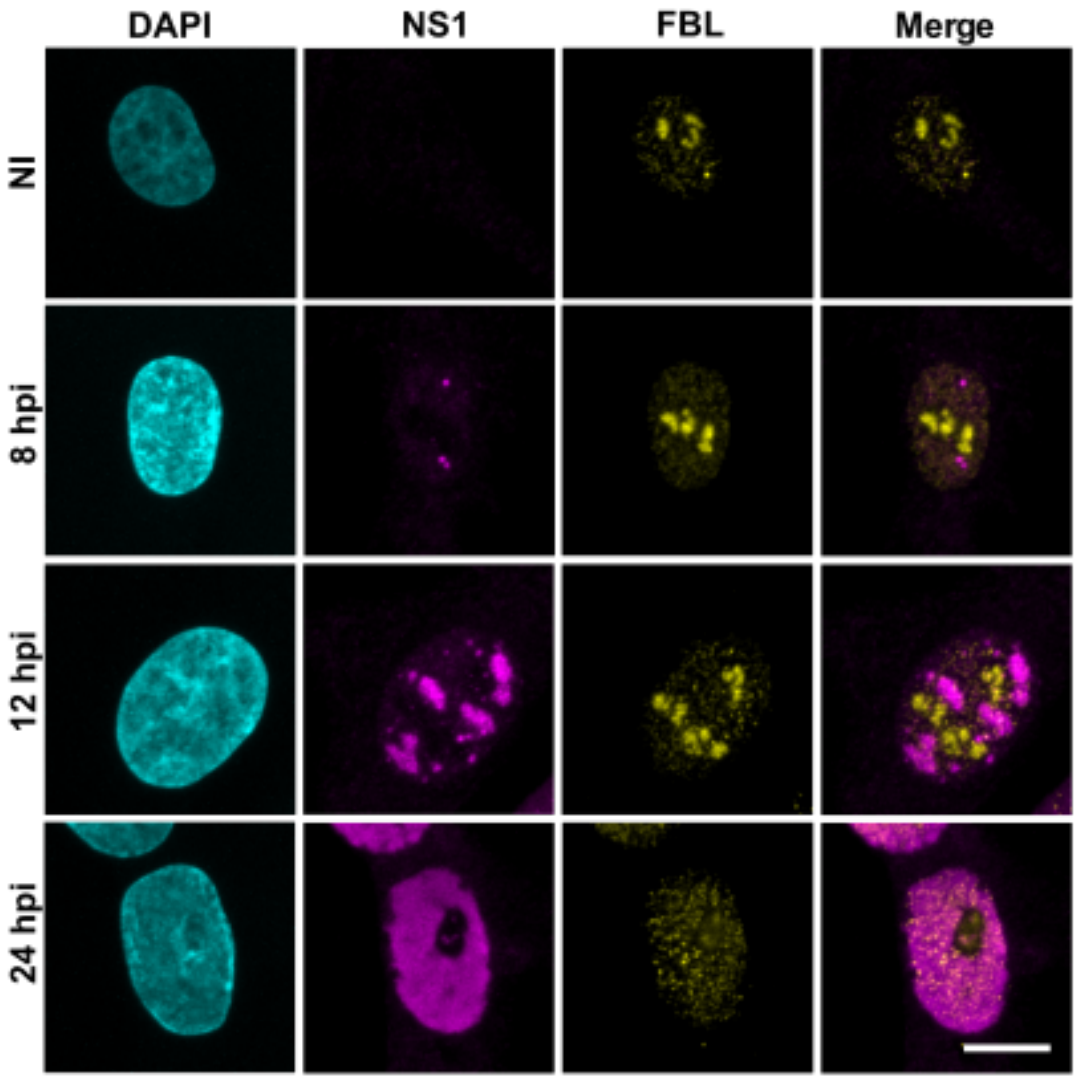

Figure S2. The inner core of the nucleolus is disassembled upon infection, leading to redistribution of fibrillarin in the nucleoplasm
Representative confocal maximum intensity projections showing the nucleolar localization of DFC marker protein, fibrillarin (FBL), in noninfected and infected NLFK cells at 8, 12, and 24 hpi. The cells were immunolabeled with fibrillarin (FBL, yellow) and the viral NS1 protein (magenta) antibodies. DNA was labeled with DAPI (cyan). Scale bar, 10 µm.

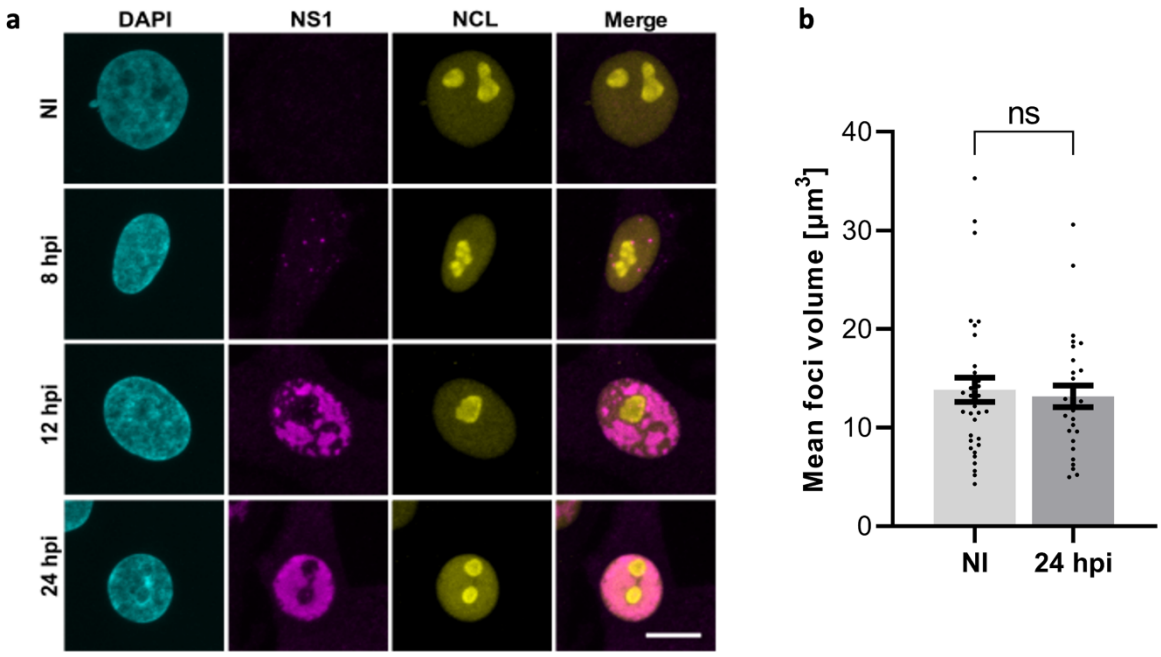

Figure S3. The periphery of the nucleolus is not disassembled upon infection
(**a**) Representative confocal maximum intensity projections showing the localization of peripheral PDFC marker protein, nucleolin (NCL), in noninfected and infected NLFK cells at 8, 12, and 24 hpi. The cells were immunolabeled with nucleolin (NCL, yellow) and the viral NS1 protein (a marker of viral replication compartment region, magenta) antibodies. DNA was labeled with DAPI (cyan). Scale bar, 10 µm. (**b**) The volume of NCL foci in noninfected and infected cells at 24 hpi (n = 34 and 29, respectively). The error bars show the standard error of the mean. No statistically significant difference was observed by Welch's *t*-test (p=0.6927)

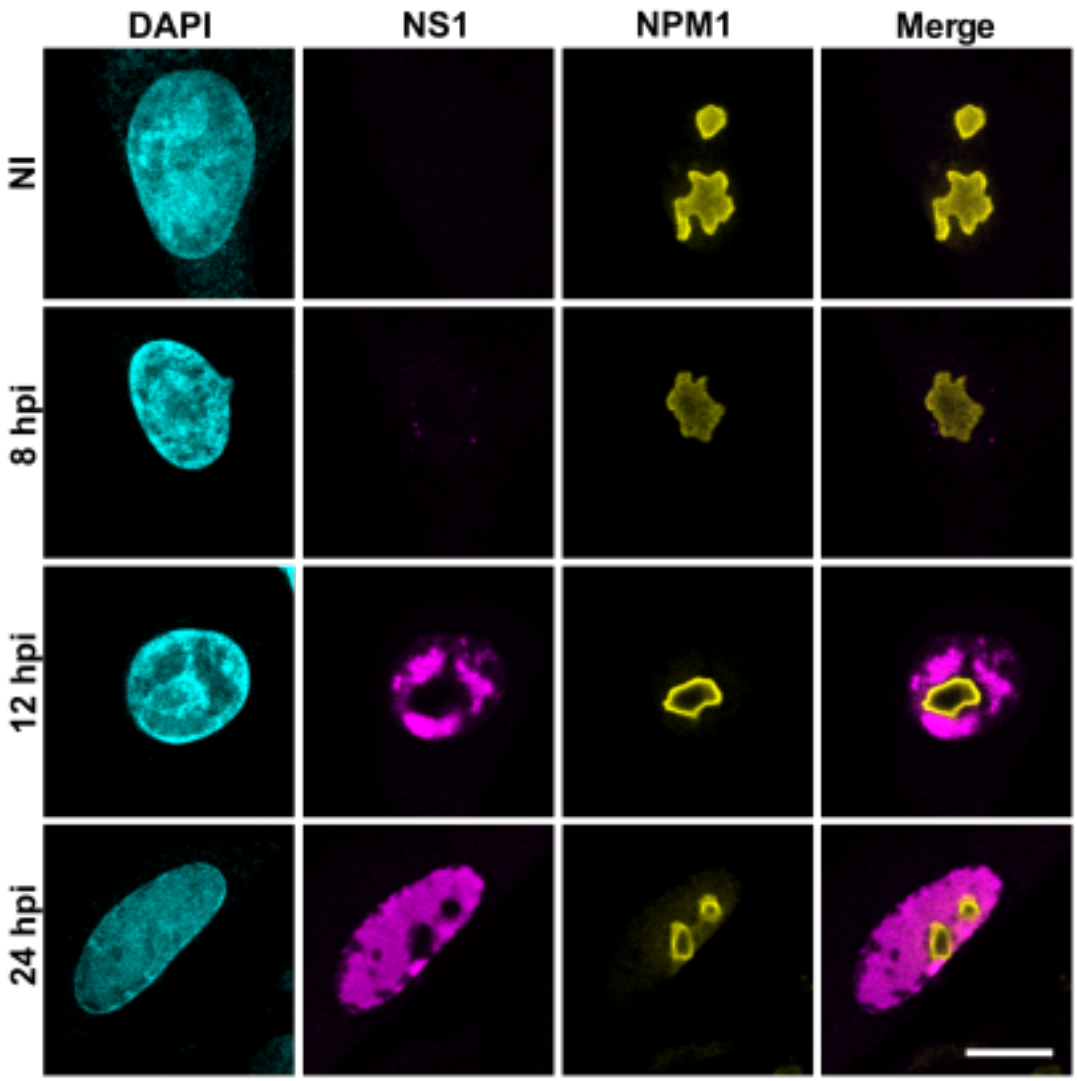

Figure S4. The periphery of the nucleolus is not disassembled upon infection
Representative confocal images of cellular localization of GC marker protein, nucleophosmin 1 (NPM1), in noninfected and infected NLFK cells at 8, 12, and 24 hpi. The cells were immunolabeled with NPM1 (yellow) and the viral NS1 protein (magenta) antibodies. DNA was labeled with DAPI (cyan). Scale bar, 10 µm.

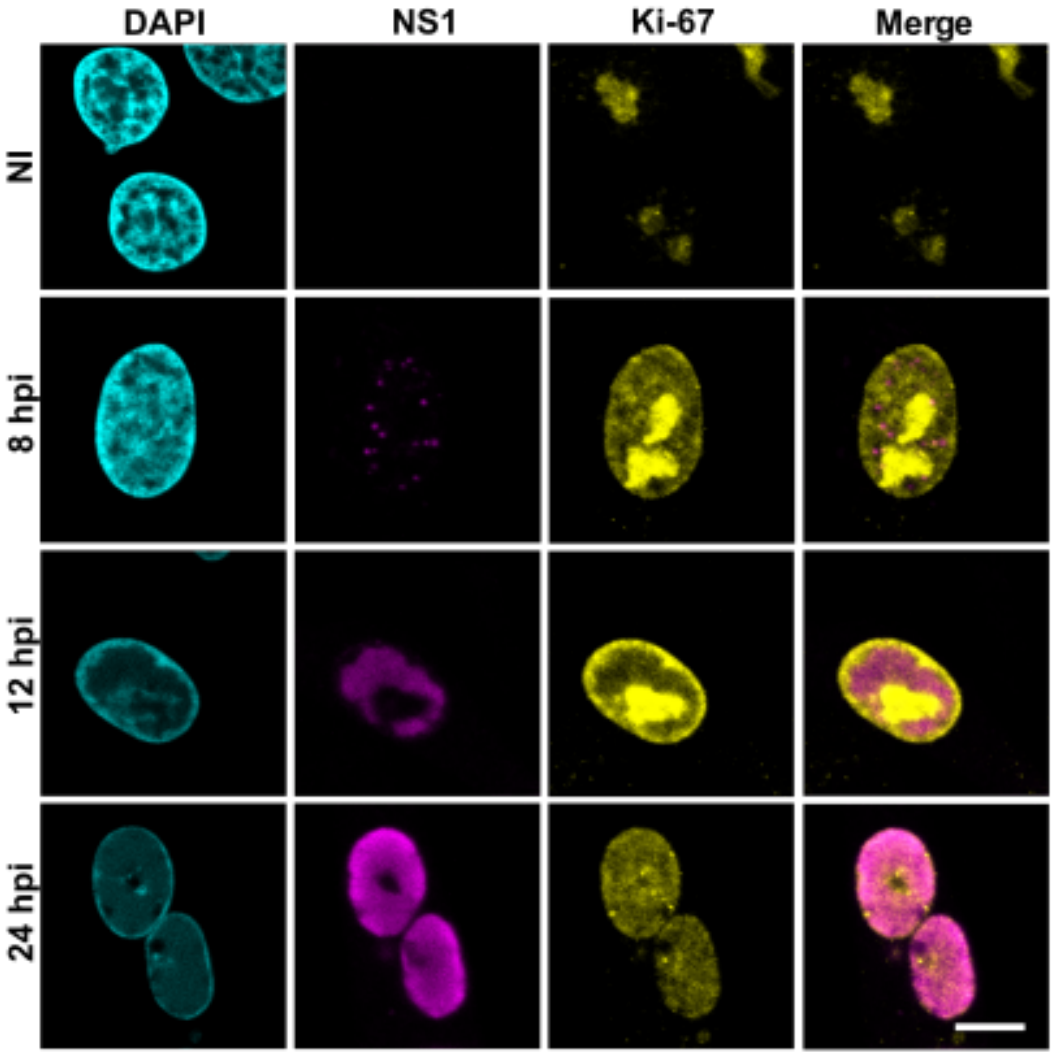

Figure S5. The nucleolar rim protein Ki-67 looses its association with the nucleolus at late infection

Representative confocal images of cellular localization of NR marker protein, Ki-67, in noninfected and infected NLFK cells at 8, 12, and 24 hpi. Scale bar, 10 µm. The cells were immunolabeled with Ki-67 (yellow) and the viral NS1 protein (magenta) antibodies. DNA was labeled with DAPI (cyan). Scale bar, 10 µm. Note that at 12 hpi, Ki-67 is strikingly redistributed at the nuclear envelope (see text for details).

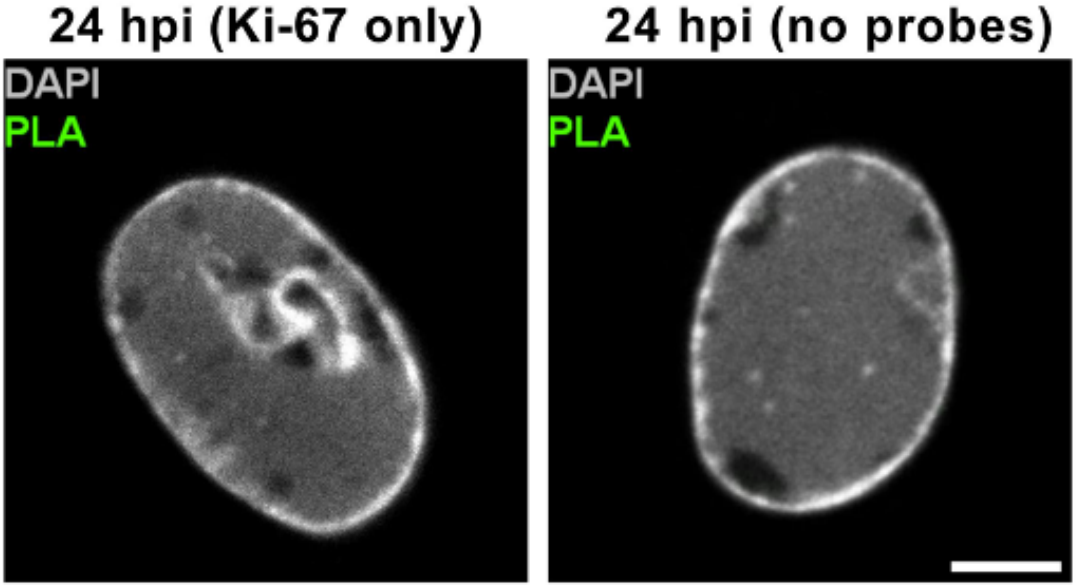

Figure S6. Technical controls for proximity ligation assay
Representative microscopy images of the technical controls for proximity ligation assay (PLA) are shown. Controls were performed with only Ki-67 antibody or without probes in 24 hpi infected cells. PLA foci in green and DAPI in grey. Scale bars, 5 µm.

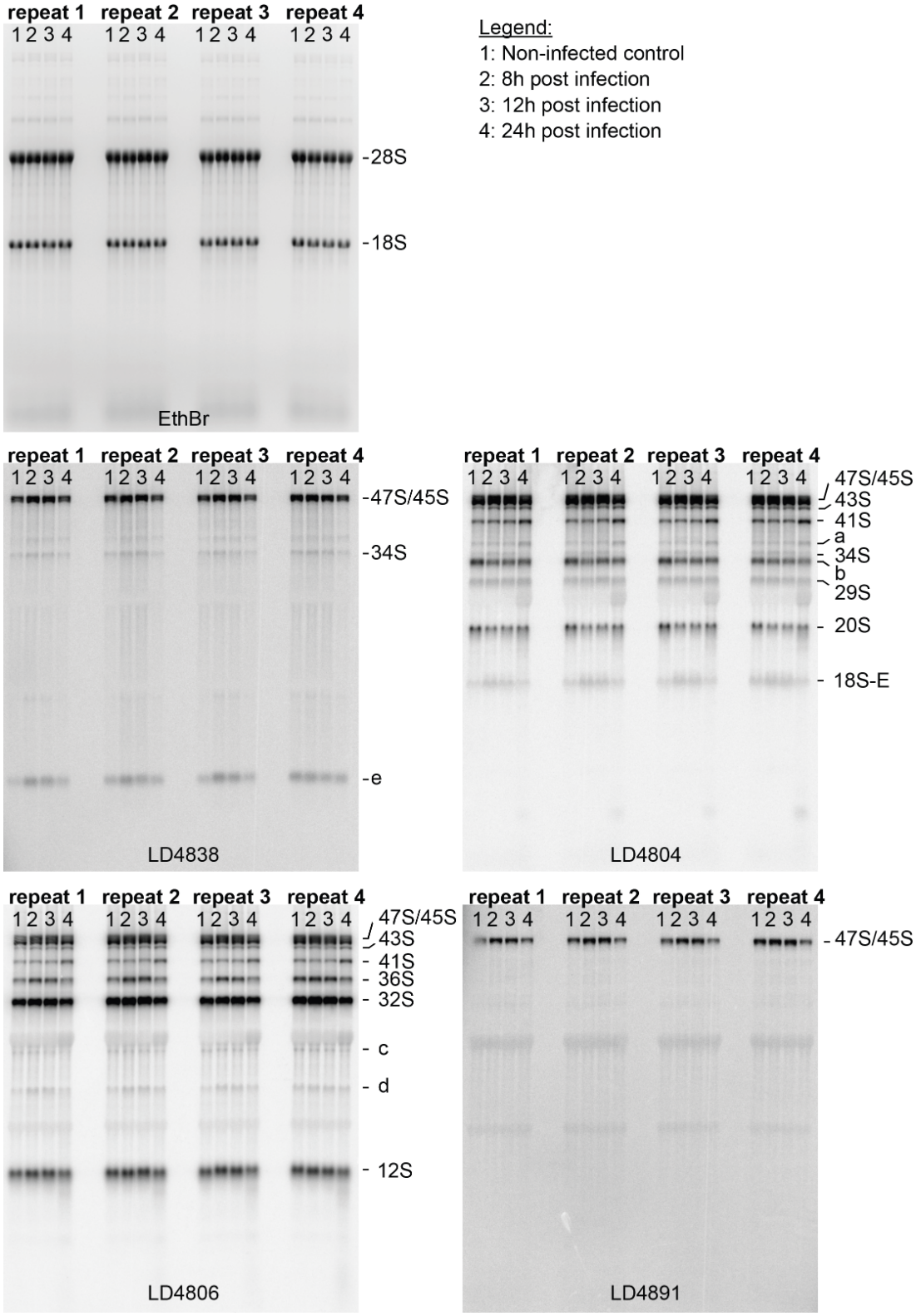

Figure S7. Pre-rRNA analysis of infected cells (4 independent biological samples)
Agarose gel analysis of ethidium bromide-stained gel (a) and northern blotting (panel b-e, see Figure 7 legend for details of probes used). Total RNA was extracted at 8, 12, and 24 hpi. A noninfected (NI) sample was used as a control. The analysis of four independent biological replicates attests to the robustness of our observations.

Noninfected	Infected spectral count	GC Loc	FC loc.	Rim loc.	Full localization	Description
76,5	78,5				Nucleoplasm, Nucleoli rim, Nuclear bodies, Mitotic chromosome	Marker of proliferation Ki-67
34	31,5				Nucleoplasm, Nucleoli fibrillar center	Ribonucleic acid export 1
27,5	20,5				Nucleoplasm, Nucleoli fibrillar center	SWI/SNF related, matrix associated, actin dependent regulator of chromatin,
13,5	13				Nucleoli	DEAD-box helicase 27
17	10,5				Nucleoplasm, Nucleoli	DNA topoisomerase II alpha
12,5	10,5				Nucleoli, Nucleoli rim, Mitotic chromosome	EBNA1 binding protein 2
11	10				Nucleoli, Cytosol	DEAD-box helicase 24
7	9				Nucleoli, Endoplasmic reticulum	Eukaryotic translation initiation factor 2 subunit beta
0	8				Nucleoplasm, Nucleoli, Nucleoli rim, Mitotic chromosome	Surfeit 6
7,5	7,5				Nucleoplasm, Nucleoli, Mitotic chromosome	RNA binding motif protein 34
6,5	7,5				Nucleoplasm, Nucleoli, Golgi apparatus	DEAD-box helicase 54
9	6,5				Nucleoplasm, Nucleoli	Structural maintenance of chromosomes 2
5	6,5				Nucleoplasm, Nucleoli	PHD finger protein 6
0	6,5				Nucleoplasm, Nucleoli, Nucleoli rim, Mitotic chromosome	Coiled-coil domain containing 86
11	6				Nucleoplasm, Nucleoli fibrillar center	SPT16 homolog, facilitates chromatin remodeling subunit
5,5	5				Nucleoplasm, Nucleoli	REX4 homolog, 3-5 exonuclease
0	4,5				Nucleoplasm, Nucleoli, Nucleoli fibrillar center	Nucleolar and spindle associated protein 1
3,5	4				Nucleoli, Mitotic chromosome	DEAD-box helicase 56
3,5	4				Nucleoplasm, Nucleoli	Serine and arginine rich splicing factor 9
3	4				Nucleoplasm, Nucleoli fibrillar center	Ubiquitin conjugating enzyme E2 N
4	3				Nucleoli, Cytosol	N-alpha-acetyltransferase 10, NatA catalytic subunit
3,5	3				Nucleoli	Ribosome biogenesis regulator 1 homolog
2,5	3				Nucleoli rim, Golgi apparatus	PWP1 homolog, endonuclein
2,5	3				Nucleoli, Nucleoli rim, Nuclear speckles	Ubiquitin specific peptidase 36
3,5	2,5				Nucleoli, Nucleoli rim, Mitotic chromosome	Nucleolar protein interacting with the FHA domain of MKI67
0	2				Nucleoplasm, Nucleoli fibrillar center	Zinc finger protein 280C
0	2				Nucleoli, Mitochondria	Mitochondrial ribosomal protein S31
21,5	0				Nucleoli rim, Mitotic chromosome	Ribosomal L1 domain containing 1
9	0				Nucleoli, Midbody	N-acetyltransferase 10
6	0				Nucleoli	RNA binding motif protein 28
6	0				Nucleoplasm, Nucleoli	NFKB repressing factor
4	0				Nucleoplasm, Nuclear membrane, Nucleoli	MRT4 homolog, ribosome maturation factor
4	0				Nucleoplasm, Nucleoli, Mitotic chromosome	BMS1 ribosome biogenesis factor
3	0				Nuclear membrane, Nucleoli	GLE1 RNA export mediator
3	0				Nucleoli	KRI1 homolog
2,5	0				Nucleoli, Mitotic chromosome	Nucleolar protein 8
2,5	0				Nucleoplasm, Nucleoli, Nucleoli rim	Ribosomal L24 domain containing 1
2,5	0				Nucleoplasm, Nuclear membrane, Nucleoli, Nucleoli rim	UTP18 small subunit processome component

Table T1. BioID hits linking NS2 to nucleolar organization and rRNA processing

The table presents 122 NS2-binding nucleolar proteins detected as high-confidence (BFDR ≤0.05) interactors. NS2-associated proteins localized in the fibrillar center (including FC and DFC, green), the granular component (GC, blue), and the nucleolar rim (NR, yellow) are highlighted.

P21333	FLNA	287	255,5	0,76	0,76
P12270	TPR	165	160,5	0,75	0,75
Q09666	AHNAK	156	131,5	0,76	0,76
P50990	CCT8	105	110	0,76	0,76
Q13085	ACACA	86,5	105,5	0,76	0,76
P49327	FASN	89	107	0,76	0,76
P78371	CCT2	71,5	83,5	0,76	0,76
P11498	PC	72	90	0,76	0,76
P46013	MKI67	78,5	76,5	0,02	0,04
P0DMV9	HSPA1B	69,5	71,5	0	0
P49368	CCT3	66	74	0,76	0,76
Q99832	CCT7	62	71,5	0,76	0,76
Q9HCC0	MCCC2	58,5	74	0,76	0,76
O75369	FLNB	76,5	72	0,76	0,76
P17987	TCP1	58	65,5	0,76	0,76
P48643	CCT5	63	65,5	0,76	0,76
P50991	CCT4	55,5	61	0,76	0,76
Q14839	CHD4	53,5	63,5	0,76	0,76
P49790	NUP153	52,5	58,5	0,67	0,66
P40227	CCT6A	53,5	60	0,76	0,76
P35658	NUP214	65,5	60,5	0,44	0,56
P49792	RANBP2	50	63	0,76	0,76
P08238	HSP90AB1	44,5	50,5	0,73	0,71
Q9Y5K6	CD2AP	52,5	54	0,76	0,76
Q96RQ3	MCCC1	46	55	0,76	0,76
P11142	HSPA8	56	48,5	0,76	0,76
P07437	TUBB	34,5	50	0,76	0,75
P27816	MAP4	41	40	0,73	0,73
P68371	TUBB4B	10,5	23,5	0,76	0,75
Q8WWM7	ATXN2L	40,5	41	0,76	0,76
O15027	SEC16A	37,5	42,5	0,64	0,59
P46821	MAP1B	42,5	45,5	0,75	0,75
Q9NR30	DDX21	41	39,5	0,71	0,71
P05165	PCCA	38,5	43	0,76	0,76
P78406	RAE1	31,5	34	0	0
Q9ULH7	MKI2	46	44,5	0,74	0,74
P35579	MYH9	45,5	39,5	0,76	0,76
Q9BVA1	TUBB2B	8	41,5	0,71	0,38
Q00839	HNRNPU	36	38	0,61	0,53
P19338	NCL	35	35,5	0,73	0,73
Q14980	NUMA1	38,5	39	0,6	0,65
P07814	EPRS	35,5	40	0,53	0,51
P07900	HSP90AA1	29	35	0,74	0,73
Q14204	DYNC1H1	37	53,5	0,14	0
Q15652	JMJD1C	32,5	35	0,75	0,75
P52948	NUP98	34	29,5	0	0
P68104	EEF1A1	23,5	31	0,74	0,73
P49321	NASP	38	34,5	0,74	0,75
Q9Y520	PRRC2C	33,5	35	0,71	0,72
Q08211	DHX9	29,5	41	0,12	0
Q14247	CTTN	28,5	30	0,73	0,73
P51610	HCFC1	37	32,5	0,76	0,76
A8CG34	POM121C	30,5	30,5	0	0
P78527	PRKDC	42	50	0,15	0,03
Q02878	RPL6	27	26,5	0,62	0,66
Q71U36	TUBA1A	19	36	0,73	0,73
P68363	TUBA1B	31,5	36	0,75	0,75
P11021	HSPA5	33	33	0,76	0,76
P23588	EIF4B	21	27,5	0,72	0,69

Table T2. Unfiltered NS2 BioID data

Unfiltered SaintExpress-analyzed BioID data was used in this study. For each identified prey protein, the average spectral count in infected and noninfected samples and BFDR values used later for filtering the dataset are shown for each identified prey protein. NS2-associated proteins localized in the fibrillar center (including FC and DFC, green), the granular component (GC, blue), the nucleolar rim (NR, yellow), and dual localization are highlighted.

	NI				8h				12h				24h			
	repeat 1	repeat 2	repeat 3	repeat 4	repeat 1	repeat 2	repeat 3	repeat 4	repeat 1	repeat 2	repeat 3	repeat 4	repeat 1	repeat 2	repeat 3	repeat 4
47/45S	100	100	100	100	169,286	135,7302	148,6536	107,9137	154,8281	122,6799	142,6578	94,90255	100,8738	75,39127	79,09903	64,30051
43S	100	100	100	100	115,8383	126,4715	135,6607	113,9038	123,5182	118,1698	138,0738	134,5062	158,7716	124,3611	148,7264	107,7192
41S	100	100	100	100	114,336	110,8312	97,57521	87,06759	116,9598	115,3307	106,7936	90,84584	166,3686	156,6136	171,7586	141,814
36S	100	100	100	100	206,4571	199,9681	221,9378	119,8173	193,2218	188,352	186,5359	113,0038	108,9705	87,65932	120,5288	66,13906
a	100	100	100	100	118,8717	94,81078	113,8789	94,37916	110,7047	107,5448	119,0437	116,9268	204,8942	204,6481	254,604	182,6271
34S	100	100	100	100	239,7041	138,5013	175,0727	127,7433	175,2389	139,836	124,8417	87,84495	49,79425	47,69279	70,85829	37,53779
b	100	100	100	100	61,68003	66,11634	66,36844	85,4191	69,98606	77,61342	69,86679	86,35694	75,41991	71,32259	68,96957	77,69712
32S	100	100	100	100	123,8055	117,8634	119,9649	109,1628	120,9669	116,9632	129,525	101,8021	92,49211	78,41256	92,59588	73,35051
29S	100	100	100	100	99,03387	93,58366	88,17305	101,0511	109,5281	113,5527	89,11928	92,8465	114,5984	124,0442	80,44483	87,98488
c	100	100	100	100	108,1299	104,9379	122,6973	108,6363	105,1943	85,90113	144,7416	104,3847	147,3998	113,4683	221,0146	144,4951
20S	100	100	100	100	61,4487	56,77871	54,01843	63,37195	68,43378	60,40111	57,38435	62,16333	86,59598	82,10931	75,4248	91,37514
d	100	100	100	100	219,5055	235,5486	175,7999	131,561	221,3857	209,7213	175,738	127,8241	139,6901	153,8977	124,9097	97,60438
18S-E	100	100	100	100	186,1603	202,3588	186,9582	142,6065	170,4068	194,2967	183,2518	136,0523	111,5568	119,9861	102,2132	73,02175
12S	100	100	100	100	131,8019	117,8357	127,9117	112,1074	132,4346	120,5108	126,1694	102,4515	103,945	92,19067	87,99138	78,7691
e	100	100	100	100	240,7474	185,2484	194,1	375,1148	212,3285	164,9511	202,686	283,0714	147,3839	127,3914	124,4762	261,063

Table T3. Quantification of rRNA processing in infection
Agarose gel analysis data of EthBr-stained RNA of noninfected (NI) and infected cells at 8, 12, and 24 hpi. The analysis of four independent biological replicates.

Movie M1. Infection-induced alteration of nucleolar structure
Expansion microscopy images and their 3D reconstructions of noninfected and infected NLFK cells at 24 hpi (see Figure 3). The surface rendering of the segmented whole nucleolus (grey), the low-intensity protein regions (green) based on the total protein staining, and DNA (blue) are shown. Specifically, interconnected low-intensity protein channel networks and infection-induced large spherical vacuolar cavities are visible.

Movie M2. Structural changes in nucleoli of infected cells
3D cryo SXT images and their reconstructions of noninfected and infected NLFK cells at 24 hpi (see Figure 4). The localization of the nucleus (blue) and nucleoli (green) are shown. Specifically, the number of small, low-density foci increases during infection.